Thermo-hydro-mechanical-chemical couplings controlling CH_4 production and CO_2 sequestration in enhanced coalbed methane recovery

Chaojun Fan [a, b, c, *], Derek Elsworth [c], Sheng Li [a, **], Lijun Zhou [a, b], Zhenhua Yang [a], Yu Song [c, d]

[a] College of Mining, Liaoning Technical University, Fuxin, Liaoning Province, China
[b] State Key Laboratory Cultivation Base for Gas Geology and Gas Control, Henan Polytechnic University, Jiaozuo, Henan Province, China
[c] Energy and Mineral Engineering, G3 Center and EMS Energy Institute, Pennsylvania State University, University Park, PA, USA
[d] School of Resources and Geosciences, China University of Mining and Technology, Xuzhou, Jiangsu province, China

ARTICLE INFO

ABSTRACT

We explore the fully coupled thermo-hydro-mechanical-chemical (THMC) response of CO_2 enhanced CBM recovery (CO_2-ECBM) considering the coupling relationships of competitive sorption of binary gas and dissolved gas in water (C), gas and water transport in two phase flow (H), thermal expansion and non-isothermal gas sorption (T), and coal deformation (M). The THMC model is developed, validated then applied to simulate CO_2 enhanced recovery. Parametric studies are completed, systematically switching-off components of the thermal (T) and hydraulic (H) coupling, to provide insights into key processes controlling ECBM recovery and key factors. The evolution of permeability is strongly dependent on coal matrix swelling/shrinkage induced by gas adsorption/desorption, expansion by thermal effects, and compaction by effective stress. Reservoir permeability first decreases, then rebounds before continuously decreasing to low magnitude. Ignoring the impact of water migration overestimates CH_4 production, and ignoring heat transfer underestimates. The high injection pressure and initial permeability will promote fluid mixture transport, resulting in an increase in production and sequestration; conversely, high injection temperature and water saturation will result in a decrease. Delaying injection start time is shown to counter the low average production rate and early CO_2 breakthrough resulting from early injection (beginning at ~2500 days for this case).

© 2019 Published by Elsevier Ltd.

1. Introduction

Coalbed methane (CBM) is an important unconventional hydrocarbon resource that has significantly gained popularity in recent decades with fuel substitution for coal resulting in significant reductions in CO_2 emissions [1—5]. Geological storage of CO_2 in unmineable coal seams is one effective way to reduce greenhouse gas emissions and enhance CBM production - utilizing CO_2 displacement and sweeping [2,6—8] leading to the popularity of CO_2 enhanced coalbed methane (CO_2-ECBM) recovery [9—11]. Since the first field trial of CO_2-ECBM in the San Juan Basin (1993), a

number of field pilots of CO_2 injection in coal seams have been conducted worldwide, such as in America, Europe, China, Japan, New Zealand, and India [12—19]. These demonstrations have been constrained by parallel experimental efforts to define key controls on ill-constrained *in situ* processes [20—23]. However, CO_2-ECBM recovery is not yet a mature technology, in spite of the growing number of pilot and field tests worldwide that have shown its potential and highlighted its difficulties [24]. The enhanced effects observed in pilot wells and those in experiments differ - largely due to the varied effects of coal reservoir properties and injection parameters, such as reservoir/injection pressure, initial/injected temperature, moisture, mineral content, pore microstructures and permeability [25—28]. Because of the lack of repeatability apparent between observations and experiments and the innate complexity of both field and laboratory tests, physics-based models that incorporate all key processes involved in the thermo-hydro-

mechanical-chemical (THMC) response in a clear and transparent manner are particularly important [29,30].

A variety of mathematical models are available to provide the necessary physics-based insight into primary and CO_2 enhanced CBM recovery [31—55]. The coal seam is typically assumed as a dual-porosity system with micro-porous matrix and macro-porous cleats/fractures containing adsorbed and free gas where the coal-gas interactions may be investigated [31—33]. The varying of in-situ stress, gas pressure and binary gas (CH_4, CO_2) sorption changes the porosity and permeability within the coal seam, which in turn impacts the evolution of binary gas diffusion and transport [34—40]. Based on these assumptions, models coupling gas flow and geomechanical processes were first proposed for enhanced coal seam methane recovery through CO_2 sequestration, in which the modified Langmuir equation is adopted for competitive sorption of binary gases, and Fick's law and Darcy's law are applied for gas diffusion and seepage in the dual-porosity system [41,42]. These include the Klinkenberg effect on gas flow [43]. Field demonstration projects have indicated the role of preexisting formation water, heterogeneous permeability and thermal effects on gas sorption − identifying a large deviation in gas production from CO_2-ECBM where these effects are not accommodated [2,25,44—48]. Hence, additional mechanistic couplings, for example gas water two-phase flow and poromechanics [3,49,50], non-isothermal gas sorption on coal [51,52] and heat transfer within fractured porous media [53] are also accommodated in representing primary and enhanced CBM recovery. In addition, studies have observed a significant reduction in the elastic modulus and permeability of coal after adsorbing carbon dioxide, demonstrating the complex couplings among the chemical, flow and mechanical properties during CO_2-ECBM recovery [54,55]. In general, these couplings provide a useful theoretical foundation for CO_2-ECBM modeling. But, these established models were either not fully coupled or one or more critical interactions were ignored. These include the incorporation of temperature dependent viscosity of gas mixtures, the role of binary gas transport and sorption between matrix and fractures, thermal effects on binary gas sorption, dissolved gas in water, and two-phase flow in water rich reservoir. A more comprehensive model coupling all these responses should be proposed to explore CH_4 production and the potential for CO_2 sequestration in enhanced CBM recovery.

We present an improved THMC coupling model for CO_2-ECBM recovery, that includes dual porosity non-isothermal interactions of binary gas competitive sorption, gas and water two-phase flow, thermal expansion that impact the dynamic evolution of porosity and permeability. This model is first validated against historic experimental data, and then applied in a parametric analysis of CO_2 enhanced recovery *in situ*. We examine a variety of models with different coupling relationships and identify key factors that control response. Finally, the impact of the start time of CO_2 injection is explored, relative to the initiation of dewatering and CH_4 drawdown, to optimize cumulative recovery. Together, these investigations provide a better understanding of the roles of mass transport and especially of heat transfer during the entire process of CO_2-ECBM recovery.

2. Development of mathematical model for CO_2 enhanced CBM recovery

CO_2 enhanced CBM recovery involves intense feedbacks in thermo-hydro-mechanical-chemical (THMC) coupling phenomenon. The hydraulic and chemical fields involve the complex mass transport of binary gases (CO_2, CH_4) with gas-water represented as concurrent two-phase flows superposed on competitive non-isothermal adsorption and dissolved gas in water. When non-thermally equilibrated CO_2 gas is injected into the coal seam, heat transfer (e.g. thermal conduction and convection) occurs among the coal skeleton, binary gases and water mass, accompanied by energy release/adsorption associated with gas sorption/desorption, in turn impacting the thermal field. The changes in the hydraulic, chemical and thermal fields also have an impact on coal deformation, affecting porosity and permeability and influencing the convective fluxes of water, gas and energy.

Models for CO_2 enhanced CBM recovery includes governing equations representing binary transport of the gas and water mixtures, coal deformation, and thermal conduction and convection. The following assumptions are typically incorporated in the governing equations [3,10,47,48,51—53]: (1) Coal is represented as a poroelastic material with single-permeability and dual-porosity (fractures and matrix pores); (2) CH_4 and CO_2 exist and migrate simultaneously in both pores and fractures - the dry gases conform to the ideal gas law and the dissolved gases to Henry's law; (3) Water only exists and migrates in fractures, with any water vapor in the gas mixture satisfying the Kelvin-Laplace law; (4) The fracture system is saturated by the binary gas and water mixtures; (5) Transport of CH_4 and CO_2 gases in the coal seam are treated in tandem as two sequential steps: CH_4 first diffuses from the matrix to the fractures according to Fick's law, and is then transported in the fractures according to Darcy's law; conversely, CO_2 migrates in the opposite direction, first transported in the fracture network according to Darcy's law then diffusing into the matrix according to Fick's law; (6) Competitive adsorption between CH_4 and CO_2 in the coal matrix satisfies the modified Langmuir equation. A schematic of these processes representing mass transport of the gas and water mixtures during CO_2-enhanced CBM recovery is shown in Fig. 1.

2.1. Governing equations of binary gas and water transport

The free binary gas in both the fracture and matrix pore is assumed to satisfy the ideal gas law. The relationship between density of the gas mixture and gas pressure can be defined as [48,51]:

$$\rho_{gi} = \frac{M_{gi}}{RT} p_{gi} \tag{1}$$

where the subscript i represents the gas component ($i = 1$ for CH_4, and $i = 2$ for CO_2); M_{gi} is the molar mass of gas component i, g/mol; p_{gi} is the gas pressure of component i, Pa; R is gas molar constant, J/(mol·K); and T is the temperature of gas, K.

The gas content of CH_4 and CO_2 in the coal matrix consists of both free and absorbed gas components with the mass in a unit volume of matrix, is defined as [52]:

$$m_{mgi} = \phi_m \rho_{gi} + V_{sgi} \rho_c \rho_{gsi} \tag{2}$$

where φ_m is the porosity of the coal matrix; ρ_{gi} is the density of gas component i, kg/m^3; V_{sgi} is the absorbed gas content of component i, m^3/kg; ρ_s is the density of the coal skeleton, kg/m^3; ρ_{gsi} is the density of gas component i under standard conditions, kg/m^3; and p_s and T_s are the atmospheric pressure and temperature under standard conditions.

The gas volume adsorbed per unit coal mass under variable temperature can be evaluated from the modified Langmuir volume equation [47,52]:

$$V_{sgi} = \frac{V_{Li}b_i p_{mgi}}{1 + \sum_{i=1}^{2} b_i p_{mgi}} \exp\left(-\frac{c_1}{1 + c_2 p_m}\left(T - T_{ref}\right)\right) \tag{3}$$

where c_1 and c_2 are the thermal coefficients of gas sorption; V_{Li} is the Langmuir volume constant of gas component i, m³/kg; p_{Li} is the Langmuir pressure constant of gas component i, Pa; $b_i = 1/P_{Li}$; p_{mgi} is the gas pressure of component i, Pa; T_{ref} is the reference temperature for the adsorption measurement, K; and $p_m = p_{mg1} + p_{mg2}$ is

the time taken for diffusion to progress between coal matrix and fractures to desorb 63.2% of the total adsorbed gas.

Applying mass conservation to the gas contained in the coal matrix, we obtain [52]:

$$\frac{\partial m_{mgi}}{\partial t} = Q_{si} \tag{6}$$

Substituting Eqs. (1)–(5) into Eq. (6), the governing equations for CH₄ and CO₂ gas migration in the coal matrix are defined as:

$$\frac{\partial}{\partial t}\left(\underbrace{\frac{V_{Li}b_i p_{mgi}}{1 + \sum_{i=1}^{2} b_i p_{mgi}} \exp\left(-\frac{c_1}{1 + c_2 p_m}\left(T - T_{ref}\right)\right)\rho_c \frac{M_{gi}}{RT_s} p_{gsi}}_{\text{Adsorbed gas in coal matrix}} + \underbrace{\phi_m \frac{M_{gi}}{RT} p_{mgi}}_{\text{Free gas in matrix pore}}\right) = \underbrace{-\frac{1}{\tau_i}\frac{M_{gi}}{RT}\left(p_{mgi} - p_{fgi}\right)}_{\text{Gas to (or from) fracture}} \tag{7}$$

the total gas pressure in the matrix, Pa.

Binary gas transport in the coal matrix is a diffusion-dominated process. According to the basic assumptions aforementioned, CH₄ and CO₂ in the coal seam are initially in the state of dynamic sorption/desorption equilibrium. When the equilibrium state is disturbed by gas extraction or injection, the adsorbed CH₄ desorbs, and diffuses from the coal matrix to the fractures, driven by the concentration gradient. Accordingly, the injected CO₂ gas counter

Formation water, CH₄ and CO₂ gas coexist in the coal reservoir with the gas-water mixture within the fractures transported as a two-phase flow. Desorption of adsorbed CH₄ in the coal matrix provides a mass source term for the CH₄ gas migration in the fractures. Accordingly, the sorption of CO₂ in the matrix represents a mass sink for CO₂ migration in the fractures. The mass conservation equation for the fracture system can be expressed as [3,52]:

$$\begin{cases} \underbrace{\frac{\partial\left(s_g\phi_f\rho_{fgi}\right)}{\partial t} + \nabla\cdot\left(\rho_{fgi}q_{gi}\right)}_{\text{Gas phase in fracture}} + \underbrace{\frac{\partial\left(s_w\phi_f\rho_{fgdi}\right)}{\partial t} + \nabla\cdot\left(\rho_{fgdi}q_w\right)}_{\text{Dissolved gas in water phase in fracture}} = \underbrace{\frac{1}{\tau_i}\frac{M_{gi}}{RT}\left(p_{mgi} - p_{fgi}\right)}_{\text{Gas from (or to) matrix}} \\ \underbrace{\frac{\partial\left(s_w\phi_f\rho_w\right)}{\partial t} + \nabla\cdot(\rho_w q_w)}_{\text{Water phase in fracture}} + \underbrace{\frac{\partial\left(s_g\phi_f\rho_{fv}\right)}{\partial t} + \nabla\cdot\left(\rho_{fv}\sum_{i=1}^{2}q_{gi}\right)}_{\text{Water vapour in gas phase in fracture}} = 0 \end{cases} \tag{8}$$

diffuses from the fractures to the matrix pores, and adsorbs to the pore surface. In this manner, the low pressure of the CH₄ in the fractures is compensated for by flow driven from the high pressure of CO₂ in the fractures. Based on Fick's law, mass transport in coal matrix is defined as [56]:

$$Q_{si} = -\frac{3\pi^2 D_i}{L^2}\frac{M_{gi}}{RT}\left(p_{mgi} - p_{fgi}\right) \tag{4}$$

where p_{mgi} is the gas pressure of component i in the matrix, Pa; p_{fgi} is the gas pressure of component i in the fracture, Pa; D_i is the diffusion coefficient of gas component i, m²/s; and L is the cleat spacing, m. Typically, the coefficients on right hand side of the above formula can be lumped together as [48]:

$$\tau_i = \frac{L^2}{3\pi^2 D_i} \tag{5}$$

where τ_i is the desorption time of gas component i, which reflects

where s_w is the water saturation; $s_g = 1 - s_w$ is the gas saturation; φ_f is the porosity of fracture; q_{gi} is the velocity of gas component i, m/s; q_w is the velocity of the water, m/s; ρ_w is water density, kg/m³; $p_{fw} = p_{fg} - p_{cgw}$ is water pressure in the fractures, Pa; p_{cgw} is the capillary pressure, Pa; and t is time, s.

Henry's law assumes a dynamic thermal equilibrium between the dissolved gas and the dry gas, the density of the dissolved gas may be obtained from Henry's law as:

$$\rho_{fgdi} = H_{gi}\rho_{fgi} \tag{9}$$

where H_{gi} is the Henry's coefficient of gas component i.

Vapor is assumed to be in equilibrium with the liquid water. According to the Kelvin−Laplace law, the vapor density is given as [57]:

$$\rho_{fv} = \rho_{fv0}h = \rho_{fv0}\exp\left(\frac{p_{cgw}}{\rho_w R_v T}\right) \tag{10}$$

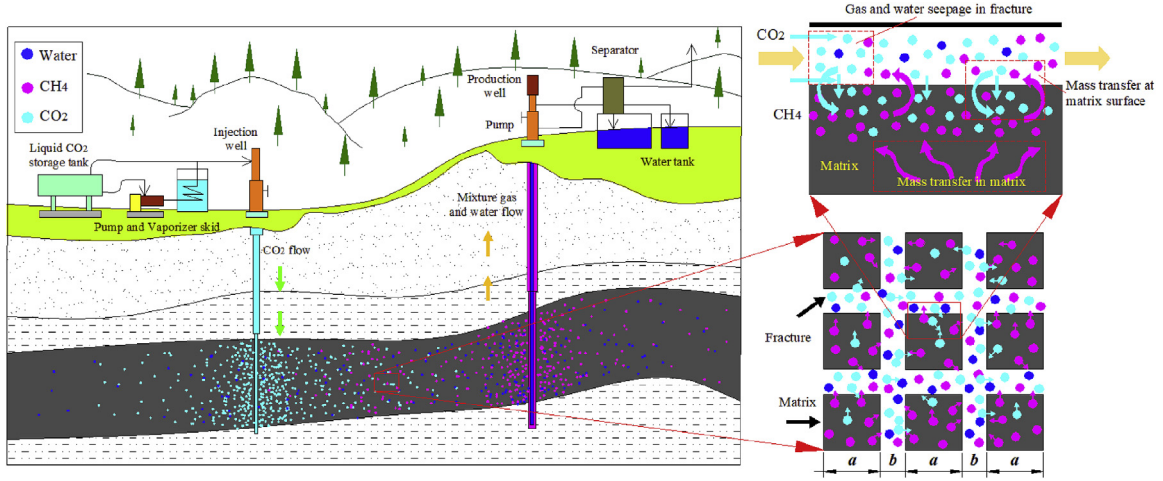where ρ_{fv0} is the density of saturated vapour, kg/m³; h is the relative

Fig. 1. Mass transport processes for gas and water mixtures during CO_2-enhanced CBM recovery.

humidity; R_v is the latent heat of vapor, J/(K·kg).

Fluid transport during CO_2 enhanced recovery involves gas-water transport as two-phase flow. By considering the Klinkenberg effect within the porous medium, the velocity of gas and water flows in the fracture can be defined by the generalized Darcy's law [3,58] as:

$$\begin{cases} q_{gi} = -\dfrac{kk_{rg}}{\mu_{gi}}\left(1+\dfrac{b_k}{p_{fgi}}\right)\nabla p_{fgi} \\[4mm] q_w = -\dfrac{kk_{rw}}{\mu_w}\nabla p_{fw} \end{cases} \tag{11}$$

$$\begin{cases} k_{rg} = k_{rg0}\left(1-\left(\dfrac{s_w-s_{wr}}{1-s_{wr}-s_{gr}}\right)\right)^2\left(1-\left(\dfrac{s_w-s_{wr}}{1-s_{wr}}\right)^2\right) \\[4mm] k_{rw} = k_{rw0}\left(\dfrac{s_w-s_{wr}}{1-s_{wr}}\right)^4 \end{cases} \tag{12}$$

where s_{wr} is the irreducible water saturation; s_{gr} is the residual gas saturation; k_{rg0} and k_{rw0} are the endpoint relative permeability of gas and water, respectively.

Substituting Eqs. (9)–(12) into Eq. (8), the governing equations for binary gas and water mixture migration in fractures can be obtained:

$$\begin{cases} \dfrac{\partial\left((1-s_w)\phi_f\rho_{fgi}\right)}{\partial t}+\nabla\cdot\left(-\dfrac{\rho_{fgi}kk_{rg}}{\mu_{gi}}\left(1+\dfrac{b_k}{p_{fgi}}\right)\nabla p_{fgi}\right)+\dfrac{\partial\left(s_w\phi_f H_{gi}\rho_{fgi}\right)}{\partial t} \\[4mm] +\nabla\cdot\left(-\dfrac{H_{gi}\rho_{fgi}kk_{rw}}{\mu_w}\nabla p_{fw}\right)=\dfrac{1}{\tau_i}\dfrac{M_{gi}}{RT}\left(p_{mgi}-p_{fgi}\right) \\[4mm] \dfrac{\partial\left(s_w\phi_f\rho_w\right)}{\partial t}+\nabla\cdot\left(-\dfrac{\rho_w kk_{rw}}{\mu_w}\nabla p_{fw}\right)+\dfrac{\partial}{\partial t}\left((1-s_w)\phi_f\rho_{fv0}\exp\left(\dfrac{p_{cgw}}{\rho_w R_v T}\right)\right) \\[4mm] +\nabla\cdot\left(-\rho_{fv0}\exp\left(\dfrac{p_{cgw}}{\rho_w R_v T}\right)\sum_{i=1}^{2}\dfrac{kk_{rg}}{\mu_{gi}}\left(1+\dfrac{b_k}{p_{fgi}}\right)\nabla p_{fgi}\right)=0 \end{cases} \tag{13}$$

where k is the absolute permeability of the coal seam, which is defined by Eq. (31), m²; k_{rw} is the water relative permeability; and k_{rg} is the gas relative permeability; μ_w is the dynamic viscosity of water, Pa·s; μ_{gi} is the dynamic viscosity of gas component i, Pa·s; and b_k is the Klinkenberg factor, Pa.

The relative permeability of the porous medium is largely dependent on the existing and residual components of the gas mixture and water. The relative permeability for gas and water (Corey) is expressed as [59–61]:

enabling mass transport of all components to be followed.

2.2. Governing equations of coal mechanical deformation

Fractured coalbeds are typical dual-porosity materials, with mechanical properties significantly influenced by the interior pores and fractures. Accommodating the expansion induced by thermal stress, the compaction induced by fluid pressure of the mixture within the matrix and fractures (effective stress), and the shrinkage/swelling resulting from gas sorption/desorption, the total strain for coal seam can be defined as [3,47,52,62]:

$$\varepsilon_{kl} = \frac{1}{2G}\sigma_{kl} - \left(\frac{1}{6G} - \frac{1}{9K}\right)\sigma_{dd}\delta_{kl} + \frac{\alpha_m p_m + \alpha_f p_f}{3K}\delta_{kl} + \frac{\alpha_T T}{3}\delta_{kl}$$
$$+ \frac{\varepsilon_s}{3}\delta_{kl}$$

$$(14)$$

where $G = D/2(1+\nu)$ is the shear modulus, Pa; ν is Poisson's ratio; $D = 1/[1/E+1/(a \cdot K_n)]$ is effective elastic modulus, Pa; K_n is the normal stiffness of the fracture, defined as the rate of change in normal stress with respect to fracture closure, Pa/m; a is the spacing between fractures, m; E is the elastic modulus, Pa; $K = D/3(1-2\nu)$ is the bulk modulus, Pa; $K_s = E_s/3(1-2\nu)$ is the skeletal bulk modulus, Pa; E_s is the skeletal elastic modulus, Pa; $\alpha_m = 1-K/K_s$ is the Biot effective stress coefficient for the coal matrix, and $\alpha_f = 1-K/(a \cdot K_n)$ is the Biot effective stress coefficient for fractures [63]; $p_m = p_{mg1}+p_{mg2}$ is the gas mixture pressure within the matrix (Dalton's law), Pa; $p_f = s_w p_{fw} + s_g (p_{fg1}+p_{fg2})$ is the water-gas mixture pressure within the fracture, Pa; α_T is the thermal expansion coefficient, 1/K; $\varepsilon_s = \varepsilon_{s1}+\varepsilon_{s2}$ is the volumetric strain of matrix swelling/shrinkage induced by gas sorption/desorption; T_0 is initial temperature within the coal seam, K; δ_{ij} is the Kronecker delta with 1 for $i=j$ and 0 for $i \neq j$.

The gas sorption/desorption in the coal matrix is usually accompanied by swelling/shrinkage within the matrix [64–66]. Experimental evidence supports the use of the extended Langmuir isotherm equation in representing the sorption of the gas mixture. By analogy, the sorption induced volume strain, in terms of each gas component, can be defined as [48,51,52]:

$$\varepsilon_{si} = \frac{\varepsilon_{Li} b_i p_{mgi}}{\left(1 + \sum_{j=1}^{2} b_j p_{mgj}\right)} \tag{15}$$

where ε_{Li} is the Langmuir-type strain coefficient, which represents the maximum swelling capacity.

The strain-deformation relation may be expressed as:

$$\varepsilon_{kl} = \frac{1}{2}\left(u_{k,l} + u_{l,k}\right) \tag{16}$$

where u_k is the deformation in the k direction, m; $k,l = $ x, y, z.

The stress equilibrium relations can be defined as:

$$\sigma_{kl,l} + f_k = 0 \tag{17}$$

$$(\rho C_p)_{eff} = \left(1 - \phi_f - \phi_m\right)\rho_s C_s + \sum_{i=1}^{2}\left(s_g \phi_f \rho_{fgi} + \phi_m \rho_{mgi} + s_w \phi_f H_{gi} \rho_{fgi}\right)C_{gi}$$
$$+ s_w \phi_f \rho_w C_w + s_g \phi_f \rho_{fv0}\exp\left(\frac{p_{cgw}}{\rho_w R_v T}\right)C_v$$

$$(20)$$

where F_k is the body force in the k direction, N.

Substituting Eqs. (14)–(16) into Eq. (17), the Navier-type equation can be obtained as:

$$\underbrace{Gu_{k,ll} + \frac{G}{1-2\nu}u_{l,lk}}_{\text{Ground stress}} - \underbrace{\left(\alpha_m p_{m,k} + \alpha_f p_{f,k}\right)}_{\text{Fluid pressure in matrix and fracture}}$$
$$- \underbrace{K\alpha_T T_{,k}}_{\text{Thermal stress}} - \underbrace{K\left(\sum_{i=1}^{2}\frac{\varepsilon_{Li} b_i p_{mgi}}{\left(1 + \sum_{j=1}^{2} b_j p_{mgj}\right)}\right)_{,k}}_{\text{Gas ad/desorption induced stress}} + \underbrace{f_k}_{\text{Coal gravity}}$$
$$= 0$$

$$(18)$$

representing the constitutive relation for both the matrix and fracture network system.

2.3. Governing equations of energy conservation

The coal skeleton, binary gas and water coexist within an REV. During the process of CH$_4$ extraction and CO$_2$ injection, energy exchange occurs due to the variation of internal energy caused by temperature change, strain energy produced by volume deformation of the coal, isosteric heat induced by gas adsorption, as well as the heat convection and conduction among the solid and fluid phases. The state of thermal equilibrium is assumed to be satisfied in this volume system, which can be expressed as [3]:

$$\underbrace{\frac{\partial}{\partial t}\left((\rho C_p)_{eff} T\right)}_{\text{Internal energy}} + \underbrace{\eta_{eff}\nabla T}_{\text{Thermal convection}} - \underbrace{\nabla \cdot \left(\lambda_{eff}\nabla T\right)}_{\text{Heat conduction}} + \underbrace{K\alpha_T T \frac{\partial \varepsilon_v}{\partial t}}_{\text{Strain energy}}$$
$$+ \underbrace{\sum_{i=1}^{2} q_{sti}\frac{\rho_s \rho_{gsi}}{M_{gi}}\frac{\partial V_{sgi}}{\partial t}}_{\text{Gas adsorption heat}}$$
$$= 0$$

$$(19)$$

where $(\rho C_p)_{eff}$ is the effective specific heat capacity of the coal mass, J/(m^3·K); η_{eff} is the effective heat convection coefficient of the fluid mixture, J/(m^2·s); λ_{eff} is the effective thermal conductivity, W/(m·K); and q_{sti} is the isosteric heat of gas adsorption of component i, kJ/mol.

The effective specific heat capacity is determined by the density and the specific heat capacity of all components within the coal mass:

where C_s, C_{g1}, C_{g2}, C_w, C_v are the specific heat capacities of coal skeleton, CH$_4$, CO$_2$, water, and vapor, J/(kg·K), respectively.

The effective heat convection coefficient of the fluid mixture is related to the convective heat transfer of CO$_2$, CH$_4$ and water in the fracture:

$$\eta_{eff} = -\sum_{i=1}^{2}\left(\frac{\rho_{fgi}C_{gi}kk_{rg}}{\mu_{gi}}\left(1+\frac{b_{ki}}{p_{fgi}}\right)\nabla p_{fgi} + \frac{H_{gi}\rho_{fgi}C_{gi}kk_{rw}}{\mu_{w}}\nabla p_{fw}\right)$$
$$-\left(\rho_{fv0}\exp\left(\frac{p_{cgw}}{\rho_{w}R_{v}T}\right)\sum_{i=1}^{2}\frac{C_{w}kk_{rg}}{\mu_{gi}}\left(1+\frac{b_{ki}}{p_{fgi}}\right)\nabla p_{fgi} + \frac{\rho_{w}C_{w}kk_{rw}}{\mu_{w}}\nabla p_{fw}\right)$$

(21)

The effective thermal conductivity of coal mass is a linear combination of the thermal conductivity of each component:

$$\lambda_{eff} = \left(1 - \phi_{f} - \phi_{m}\right)\lambda_{s} + \phi_{m}\lambda_{mgm} + \phi_{f}\left(s_{g}\lambda_{fgm} + s_{w}\lambda_{fw}\right) \quad (22)$$

where λ_{s}, λ_{mgm}, λ_{fgm}, λ_{fw} are the thermal conduction coefficients for the coal skeleton, gas mixture (CO_2 and CH_4) in the matrix, gas mixture in the fractures, and water in fractures, respectively, W/(m·K).

For the gas mixture, the thermal conduction coefficient is defined as:

$$\lambda_{m} = \frac{1}{2}\left(\sum_{i=1}^{N}x_{i}\lambda_{i} + \left(\sum_{i=1}^{N}x_{i}/\lambda_{i}\right)^{-1}\right) \quad (23)$$

where x_{i} and λ_{i} are the molar fraction and thermal conduction coefficient of gas component i, respectively; N is the number of gas components in the mixture - for the matrix $N = 2$ (CO_2 and CH_4), while for the fractures $N = 3$ (CO_2, CH_4 and vapor).

2.4. Porosity and permeability evolution

The coal seam is assumed to be a dual-porosity and single-permeability medium with matrix pores and fractures, as shown in Fig. 2. The matrix pores provide the principal reservoirs for gas storage, while the fracture porosity controls permeability and therefore significantly affects the migration of the binary gas and water mixture. Therefore, porosity and permeability exert the key controls on the entire process of CO_2-ECBM recovery, *viz* the coupling of the solid stress, gas pressure, binary gas sorption, thermal response and mechanical properties of the coal seam.

A general model of porosity in the coal matrix can be expressed as [3]:

$$\phi_{m} = \phi_{m0} + \frac{(\alpha_{m} - \phi_{m0})(\varepsilon_{e} - \varepsilon_{e0})}{(1 + \varepsilon_{e})} \quad (24)$$

where $\varepsilon_{e} = \varepsilon_{v} + p_{m}/K_{s} - \alpha_{T}T - \varepsilon_{s}$; ε_{v} is the volume strain of the coal, and the subscript '0' represents the initial value of all parameters.

The effective stress of the coal matrix and fracture are defined as [63,67]:

$$\begin{cases} \sigma_{em} = \overline{\sigma} - \left(\alpha_{m}p_{m} + \alpha_{f}p_{f}\right) \\ \sigma_{ef} = \overline{\sigma} - \alpha_{f}p_{f} \end{cases} \quad (25)$$

where $\overline{\sigma} = (\sigma_{11} + \sigma_{22} + \sigma_{3})/3$ is the average principal stress.

Considering the effective stress acting upon the coal matrix and fractures, the volumetric strain of the REV is expressed as [68]:

$$\Delta\varepsilon_{v} = \frac{a^{3}}{s^{3}K_{m}}\Delta\sigma_{em} + \frac{s^{3} - a^{3}}{s^{3}K_{f}}\Delta\sigma_{ef} - \frac{a^{3}}{s^{3}}\Delta(\varepsilon_{s1} + \varepsilon_{s2}) - \frac{a^{3}}{s^{3}}\alpha_{T}\Delta T$$

(26)

where $s = a+b$ is the length of the REV, m; a is the spacing between parallel fracture sets, m; and b is the facture aperture, m.

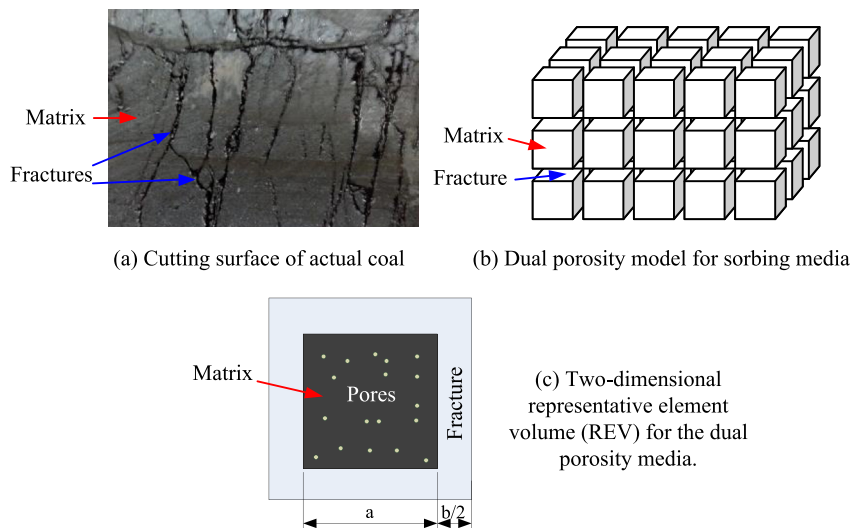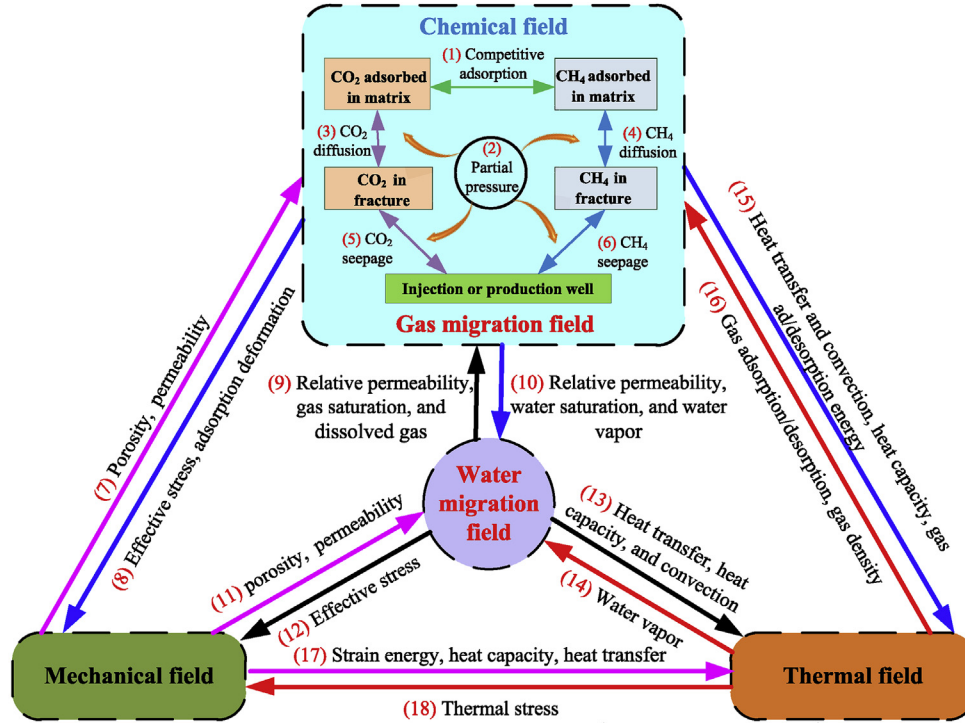Substituting Eq. (25) into Eq. (26), we obtain:

(a) Cutting surface of actual coal   (b) Dual porosity model for sorbing media

(c) Two-dimensional representative element volume (REV) for the dual porosity media.

Fig. 2. Dual-porosity and single-permeability model for a coal seam.

Chemical field

(1) Competitive adsorption

CO$_2$ adsorbed in matrix ↔ CH$_4$ adsorbed in matrix

(3) CO$_2$ diffusion

(2) Partial pressure

(4) CH$_4$ diffusion

CO$_2$ in fracture

CH$_4$ in fracture

(5) CO$_2$ seepage

(6) CH$_4$ seepage

Injection or production well

Gas migration field

(15) Heat transfer and convection, heat capacity, gas ad/desorption energy

(16) Gas adsorption/desorption, gas density

(9) Relative permeability, gas saturation, and dissolved gas

(10) Relative permeability, water saturation, and water vapor

Water migration field

(7) Porosity, permeability

(8) Effective stress, adsorption deformation

(11) porosity, permeability

(12) Effective stress

(13) Heat transfer, heat capacity, and convection

(14) Water vapor

Mechanical field

(17) Strain energy, heat capacity, heat transfer

(18) Thermal stress

Thermal field

Governing equations

Mechanical field

$$Gu_{k,ll} + \frac{G}{1-2\upsilon}u_{l,lk} - (\alpha_m p_{m,k} + \alpha_f p_{f,k}) - K\alpha_T T_{,k} - K\left(\frac{\varepsilon_{L1}b_{L1}p_{mg1} + \varepsilon_{L2}b_{L2}p_{mg2}}{(1+b_{L1}p_{mg1}+b_{L2}p_{mg2})}\right)_{,k} + f_k = 0$$

(7), (11), (17)   (8), (12)   (14)   (8)   (7), (11), (17)

Hydraulic field and chemical field

$$\frac{\partial}{\partial t}\left(\frac{V_{L1}b_1 p_{mg1}}{1+b_1 p_{mg1}+b_2 p_{mg2}}\exp\left(-\frac{c_1}{1+c_2 p_m}(T-T_{ref})\right)\rho_c \frac{M_{g1}}{RT_s}p_s + \phi_m \frac{M_{g1}}{RT}p_{mg1}\right) = -\frac{1}{\tau_1}\frac{M_{g1}}{RT}(p_{mg1}-p_{fg1})$$

(1), (2), (16)   (2), (7), (16)   (2), (4), (6), (16)

$$\frac{\partial}{\partial t}\left(\frac{V_{L2}b_2 p_{mg2}}{1+b_1 p_{mg1}+b_2 p_{mg2}}\exp\left(-\frac{c_1}{1+c_2 p_m}(T-T_{ref})\right)\rho_c \frac{M_{g2}}{RT_s}p_s + \phi_m \frac{M_{g2}}{RT}p_{mg2}\right) = -\frac{1}{\tau_2}\frac{M_{g2}}{RT}(p_{mg2}-p_{fg2})$$

(1), (2), (16)   (2), (7), (16)   (2), (3), (5), (16)

$$\frac{\partial\left(s_g\phi_f\rho_{fg1}\right)}{\partial t} + \nabla\cdot\left(-\frac{\rho_{fg1}kk_{rg}}{\mu_{g1}}\left(1+\frac{b_k}{p_{fg1}}\right)\nabla p_{fg1}\right) + \frac{\partial\left(s_w\phi_f H_{g1}\rho_{fg1}\right)}{\partial t} + \nabla\cdot\left(-\frac{H_{g1}\rho_{fg1}kk_{rw}}{\mu_w}\nabla p_{fw}\right) = \frac{1}{\tau_1}\frac{M_{g1}}{RT}(p_{mg1}-p_{fg1})$$

(2), (7), (9), (16)   (2), (6), (7), (9), (16)   (2), (7), (9), (16)   (2), (6), (7), (9), (16)   (2), (4), (6), (16)

$$\frac{\partial\left(s_g\phi_f\rho_{fg2}\right)}{\partial t} + \nabla\cdot\left(-\frac{\rho_{fg2}kk_{rg}}{\mu_{g2}}\left(1+\frac{b_k}{p_{fg2}}\right)\nabla p_{fg2}\right) + \frac{\partial\left(s_w\phi_f H_{g2}\rho_{fg2}\right)}{\partial t} + \nabla\cdot\left(-\frac{H_{g2}\rho_{fg2}kk_{rw}}{\mu_w}\nabla p_{fw}\right) = \frac{1}{\tau_2}\frac{M_{g2}}{RT}(p_{mg2}-p_{fg2})$$

(2), (7), (9), (16)   (2), (5), (7), (9), (16)   (2), (7), (9), (16)   (2), (5), (7), (9), (16)   (2), (3), (5), (16)

$$\frac{\partial\left(s_w\phi_f\rho_w\right)}{\partial t} + \nabla\cdot\left(-\frac{\rho_w kk_{rw}}{\mu_w}\nabla p_{fw}\right) + \frac{\partial}{\partial t}\left(s_g\phi_f\rho_{fv0}\exp\left(\frac{p_{cgw}}{\rho_w R_v T}\right)\right) + \nabla\cdot\left(-\rho_{fv0}\exp\left(\frac{p_{cgw}}{\rho_w R_v T}\right)\sum_{i=1}^{2}\frac{kk_{rg}}{\mu_{gi}}\left(1+\frac{b_{ki}}{p_{fgi}}\right)\nabla p_{fgi}\right) = 0$$

(10), (11)   (10), (11)   (9), (11), (14)   (7), (9), (14)

Thermal field

$$\frac{\partial}{\partial t}\left((\rho C_p)_{eff}T\right) + \eta_{eff}\nabla T - \nabla\cdot\left(\lambda_{eff}\nabla T\right) + K\alpha_T T\frac{\partial\varepsilon_v}{\partial t} + q_{st1}\frac{\rho_s\rho_{gs1}}{M_{g1}}\frac{\partial V_{sg1}}{\partial t} + q_{st2}\frac{\rho_s\rho_{gs2}}{M_{g2}}\frac{\partial V_{sg2}}{\partial t} = 0$$

(13), (15), (17)   (13), (15)   (13), (15), (17)   (17)   (15)   (15)

Cross-coupling equations

Matrix porosity
$$\phi_m = \phi_{m0} + \frac{(\alpha_m - \phi_{m0})(\varepsilon_e - \varepsilon_{e0})}{(1+\varepsilon_e)}$$

Fracture porosity
$$\phi_f = \phi_{f0}\left(1+\frac{\Delta b}{b}\right) = \phi_{f0} + \frac{\phi_{f0}K_m}{3\left(K_f r_{as}^3 + K_m - K_m r_{as}^3\right)}\left(r_{as}^3\Delta(\varepsilon_{s1}+\varepsilon_{s2}) + r_{as}^3\alpha_T\Delta T + \Delta\varepsilon_v + \frac{r_{as}^3}{K_m}\alpha_m\Delta p_m\right)$$

Permeability
$$k = k_0\left(1 + \frac{K_m}{3\left(K_f r_{as}^3 + K_m - K_m r_{as}^3\right)}\left(r_{as}^3\Delta(\varepsilon_{s1}+\varepsilon_{s2}) + r_{as}^3\alpha_T\Delta T + \Delta\varepsilon_v + \frac{r_{as}^3}{K_m}\alpha_m\Delta p_m\right)\right)^3$$

Relative permeability
$$k_{rw} = \left(\frac{S_w - S_{wr}}{1 - S_{wr}}\right)^4, \qquad k_{rg} = \left[1 - \left(\frac{S_w - S_{wr}}{1 - S_{wr} - S_{gr}}\right)\right]^2\left[1 - \left(\frac{S_w - S_{wr}}{1 - S_{wr}}\right)^2\right]$$

Fig. 3. Coupling relations of the proposed model for CO$_2$-ECBM recovery.

$$\Delta \varepsilon_v = \frac{a^3}{s^3 K_m} \Delta \left(\overline{\sigma} - \left(\alpha_m p_m + \alpha_f p_f \right) \right) + \frac{s^3 - a^3}{s^3 K_f} \Delta \left(\overline{\sigma} - \alpha_f p_f \right)$$
$$- \frac{a^3}{s^3} \Delta (\varepsilon_{s1} + \varepsilon_{s2}) - \frac{a^3}{s^3} \alpha_T \Delta T \tag{27}$$

Assuming $r_{as} = a/s$ as the ratio of matrix width to the REV length enables the effective stress on the fractures is expressed as:

$$\Delta \overline{\sigma} - \alpha_f \Delta p_f = \frac{K_m K_f}{K_f r_{as}^3 + K_m - K_m r_{as}^3} \left(r_{as}^3 \Delta(\varepsilon_{s1} + \varepsilon_{s2}) + r_{as}^3 \alpha_T \Delta T \right.$$
$$\left. + \Delta \varepsilon_v + \frac{r_{as}^3}{K_m} \alpha_m \Delta p_m \right) \tag{28}$$

The fracture deformation caused by the change in effective stress is defined as:

$$\Delta b = \frac{b}{3K_f} \Delta \sigma_{ef} = \frac{b}{3K_f} \left(\Delta \overline{\sigma} - \alpha_f \Delta p_f \right) \tag{29}$$

Therefore, the evolution of fracture porosity can be expressed as:

$$\phi_f = \phi_{f0} \left(1 + \frac{\Delta b}{b} \right)$$
$$= \phi_{f0} + \frac{\phi_{f0} K_m}{3 \left(K_f r_{as}^3 + K_m - K_m r_{as}^3 \right)} \left(r_{as}^3 \Delta(\varepsilon_{s1} + \varepsilon_{s2}) + r_{as}^3 \alpha_T \Delta T \right.$$
$$\left. + \Delta \varepsilon_v + \frac{r_{as}^3}{K_m} \alpha_m \Delta p_m \right) \tag{30}$$

The cubic law between fracture porosity and permeability is adopted,

Fig. 4. Geometric and boundary conditions for model validation.

CO_2 migration in the matrix system, three PDE modules for the migration of the gas-water mixture in the fracture system, with a

$$k = k_0 \left(1 + \frac{K_m}{3\left(K_f r_{as}^3 + K_m - K_m r_{as}^3 \right)} \left(r_{as}^3 \Delta(\varepsilon_{s1} + \varepsilon_{s2}) + r_{as}^3 \alpha_T \Delta T + \Delta \varepsilon_v + \frac{r_{as}^3}{K_m} \alpha_m \Delta p_m \right) \right)^3 \tag{31}$$

where φ_{f0} is the initial fracture porosity; and k_0 is the initial fracture permeability, m^2.

2.5. Coupling relation for the THMC model

We assemble governing Eq. (7), (13), (18), (19), (24), (30) and (31) to establish the THMC model for CO_2-ECBM recovery. The coupling relations are shown in Fig. 3. The bidirectional interactions between the coal deformation, binary gas (CO_2, CH_4) sorption and transport, water transport and heat transfer fields illustrate the full coupling of the proposed model. The equations are complex nonlinear second-order partial differential equations (PDEs) that, due to their spatio-temporal nonlinearity, are difficult to solve analytically [3]. COMSOL Multiphysics provides a powerful PDE-based modeling environment that we utilize to obtain a numerical solution using the finite element (FE) method. The solid mechanics module is applied to evaluate mechanical deformation, and several general PDE modules are applied to calculate hydraulic, thermal and chemical fields – two PDE modules are for CH_4 and
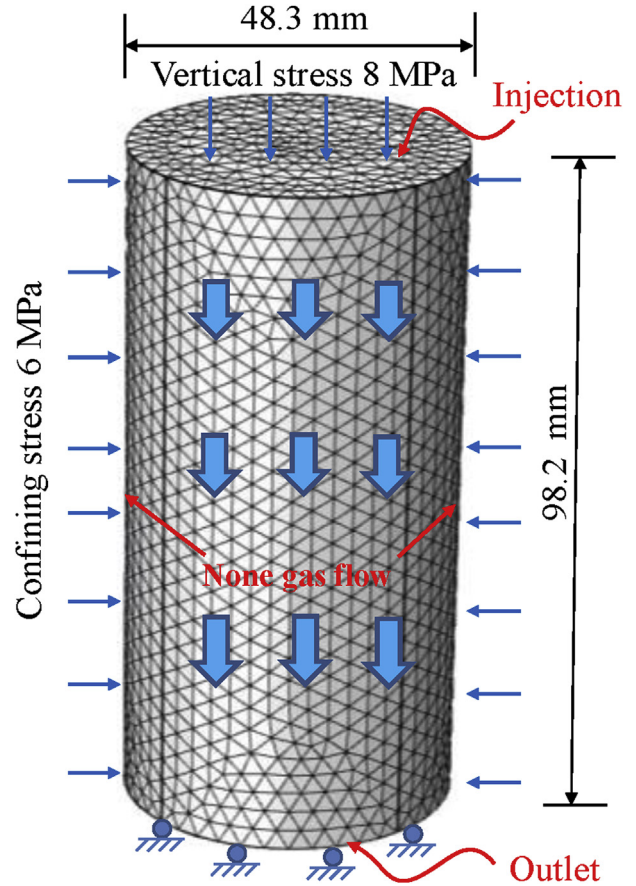
final PDE module accommodating energy transport.

3. Model validation

3.1. Parameter setting and geometry model

Results are available for a set of core flooding experiments representing CO_2-ECBM recovery [22] at a variety of injection pressures. Large coal blocks collected from the C1 coal seam of the Baijiao coal mine, south Sichuan basin, China, were shaped into cylindrical samples (48.3 mm in diameter and 98.2 mm in height). The tests were performed using a high pressure triaxial servo−controlled core holder at Chongqing University. This apparatus comprises three parts - a triaxial cell, a temperature control unit and a gas injection and recovery unit. The coal sample is first loaded into the apparatus and the temperature set to 15 °C. After removing the residual air, the sample is saturated with CH_4 at 1.5 MPa under confining stress of 6 MPa. Following equilibrium sorption (no volume change), CO_2 is then injected into the sample

and the flooding experiment conducted at CO_2 injection pressures of 2, 2.5, 3, and 3.5 MPa.

This laboratory experiment is followed using the THMC model described in the previous. The coal sample is represented as shown in Fig. 4 under a constant confining stress of 6 MPa and vertical stress of 8 MPa. CO_2 injection pressures (2, 2.5, 3, and 3.5 MPa) are applied to the top boundary with the CO_2 and CH_4 pressures at the outlet set to atmospheric pressure with no water nor gas flow across the boundaries. The initial CH_4 pressure, water saturation, permeability, and temperature in the coal sample are set to 1.5 MPa, 0.6, 1.2×10^{-17} m^2, and 15 °C, respectively. The key parameters used in modelling are listed in Table 1, with all other parameters congruent with those of the simulation of CO_2-ECBM recovery *in situ* (Table 2 in Section 4.1). The results of both experiment and modelling are shown in Figs. 5 and 6.

3.2. Results comparison

Fig. 5 shows the volume composition of CH_4 and CO_2 at the outlet relative to injection pressure for both models and measurements. The produced gas at the outlet is initially pure CH_4 with the volume composition of CH_4 successively decreasing and that of CO_2 increasing - indicating the breakthrough of CO_2. Post breakthrough, the CH_4 composition decreases and the CO_2 composition increases continuously over time. Finally, the CO_2 composition

reaches to ~90% when the outlet is closed. For injection pressures of 2, 2.5, 3, 3.5 MPa, the average relative errors of CH_4 composition are 23, 13.5, 14.2 and 24.3%, and those of CO_2 composition are 11.8, 5.4, 6.1 and 3.6%, respectively. The breakthrough time for the CO_2 shortens with an increase in the injected gas pressure − an increased CO_2 pressure gradient results in an increased CO_2 flow velocity and earlier breakthrough. For the experiments, the breakthrough time for the CO_2 under the injection pressures of 2, 2.5, 3, and 3.5 MPa are 16, 10, 6, and 4 min, respectively. For the simulations, the corresponding values are 13, 9, 5, and 4 min, respectively - indicating that the simulated results adequately match the experimental observations.

Fig. 6 compares the flow rates of CH_4 and CO_2 at the outlet between the modelling and experimental data. As anticipated, an increased injection pressure results in an increased CO_2 flow rate at the outlet and a shorter duration for the flow rate to reach peak magnitude. The CH_4 flow rate at higher injection pressures usually exhibits a relatively higher value at beginning, but drops dramatically over time. Compared to the experimental results, the CH_4 flow rate in the simulation is characterized by a process of initial transient increase, followed by a rapid decrease. This is because the gas transport in the coal sample is affected by the combined effects of competitive sorption, water seepage, heat transfer and effective stress on coal. For injection pressures of 2, 2.5, 3, 3.5 MPa, the average relative errors of CH_4 flow rate are 23.8, 24.6, 35.5 and

Table 1
Key parameters used in model validation.

Parameter	Value	Parameter	Value
Porosity of matrix (φ_m)	0.06	Initial permeability of fracture (k_0, m^2)	1.2×10^{-17}
Porosity of fracture (φ_f)	0.01	Langmuir volume constant of CH_4 (V_{L1}, m^3/kg)	0.02
Dynamic viscosity of CH_4 (μ_1, Pa·s)	1.03×10^{-5}	Langmuir pressure constant of CH_4 (P_{L1}, MPa)	2.07
Dynamic viscosity of CO_2 (μ_2, Pa·s)	1.38×10^{-5}	Langmuir volume constant of CO_2 (V_{L2}, m^3/kg)	0.0314
Dynamic viscosity of water (μ_w, Pa·s)	1.01×10^{-3}	Langmuir pressure constant of CO_2 (P_{L2}, MPa)	1.38
Initial water saturation (s_{wi})	0.6	Langmuir-type strain coefficient of CH_4 (ε_{L1})	0.0128
Irreducible water saturation (s_{wr})	0.42	Langmuir-type strain coefficient of CO_2 (ε_{L2})	0.0237

Table 2
Related parameters used in the numerical simulation.

Parameter	Value	Parameter	Value
Density of coal (ρ_c, kg/m^3)	1.47×10^3	Initial permeability of fracture (k_0, m^2)	5.14×10^{-16}
Porosity of matrix (φ_m)	0.045	Langmuir volume constant of CH_4 (V_{L1}, m^3/kg)	0.0256
Porosity of fracture (φ_f)	0.011	Langmuir pressure constant of CH_4 (P_{L1}, MPa)	2.07
Dynamic viscosity of CH_4 (μ_1, Pa·s)	1.34×10^{-5}	Langmuir volume constant of CO_2 (V_{L2}, m^3/kg)	0.0447
Dynamic viscosity of CO_2 (μ_2, Pa·s)	1.84×10^{-5}	Langmuir pressure constant of CO_2 (P_{L2}, MPa)	1.38
Dynamic viscosity of water (μ_w, Pa·s)	1.01×10^{-3}	Langmuir constant of CH_4 induced strain (ε_{L1})	0.0128
Capillary pressure (p_{cgw}, MPa)	0.035	Langmuir constant of CO_2 induced strain (ε_{L2})	0.0237
Thermal coefficients of gas sorption (c_1, 1/T)	0.021	Endpoint relative permeability of water (k_{rw0})	1.0
Thermal coefficients of gas sorption (c_2, 1/MPa)	0.071	Endpoint relative permeability of gas (k_{rg0})	0.875
Isosteric heat of CH_4 adsorption (q_{st1}, kJ/mol)	16.4	Initial water saturation (s_{wi})	0.82
Isosteric heat of CO_2 adsorption (q_{st2}, kJ/mol)	19.2	Irreducible water saturation (s_{wr})	0.42
Initial temperature in coal seam (T_0, K)	305.5	Residual gas saturation (s_{gr})	0.05
Young's modulus of coal seam (E, GPa)	2.713	Klinkenberg factor (b_k, MPa)	0.76
Young's modulus of coal skeleton (E_s, GPa)	8.469	Initial CO_2 gas pressure in fracture (p_{fg20}, MPa)	0.1
Fracture stiffness (K_n, GPa/m)	2.8	Initial CO_2 gas pressure in matrix (p_{mg20}, MPa)	0.1
Poisson's ratio of coal (ν)	0.35	Initial CH_4 gas pressure in fracture (p_{fg10}, MPa)	5.24
Specific heat capacity of coal (C_s, J/(kg·K))	1350	Initial CH_4 gas pressure in matrix (p_{mg10}, MPa)	5.24
Specific heat capacity of water (C_w, J/(kg·K))	4187	Adsorption time of CH_4 (τ_1, d)	0.221
Specific heat capacity of CH_4 (C_{g1}, J/(kg·K))	2220	Adsorption time of CO_2 (τ_2, d)	0.334
Specific heat capacity of CO_2 (C_{g2}, J/(kg·K))	844	Thermal conductivity of coal (λ_s, W/(m·K))	0.1913
Specific heat capacity of vapor (C_v, J/(kg·K))	1996	Thermal conductivity of CH_4 (λ_{g1}, W/(m·K))	0.0301
Thermal expansion coefficient of coal (α_T, 1/K)	2.4×10^{-5}	Thermal conductivity of CO_2 (λ_{g2}, W/(m·K))	0.0137
Reference temperature for adsorption test (T_{ref}, K)	300	Thermal conductivity of water (λ_w, W/(m·K))	0.5985
Density of saturated water vapor (ρ_{fv0}, kg/m^3)	0.13	Gas constant of water vapor, (R_v, J/(K·kg))	461.51
Henry's coefficient of CH_4 (H_{g1})	0.0014	Langmuir-type strain coefficient of CH_4 (ε_{L1})	0.0128
Henry's coefficient of CO_2 (H_{g2})	0.0347	Langmuir-type strain coefficient of CO_2 (ε_{L2})	0.0237

(a) p_{inj}=2 MPa

(b) p_{inj}=2.5 MPa

(c) p_{inj}=3 MPa

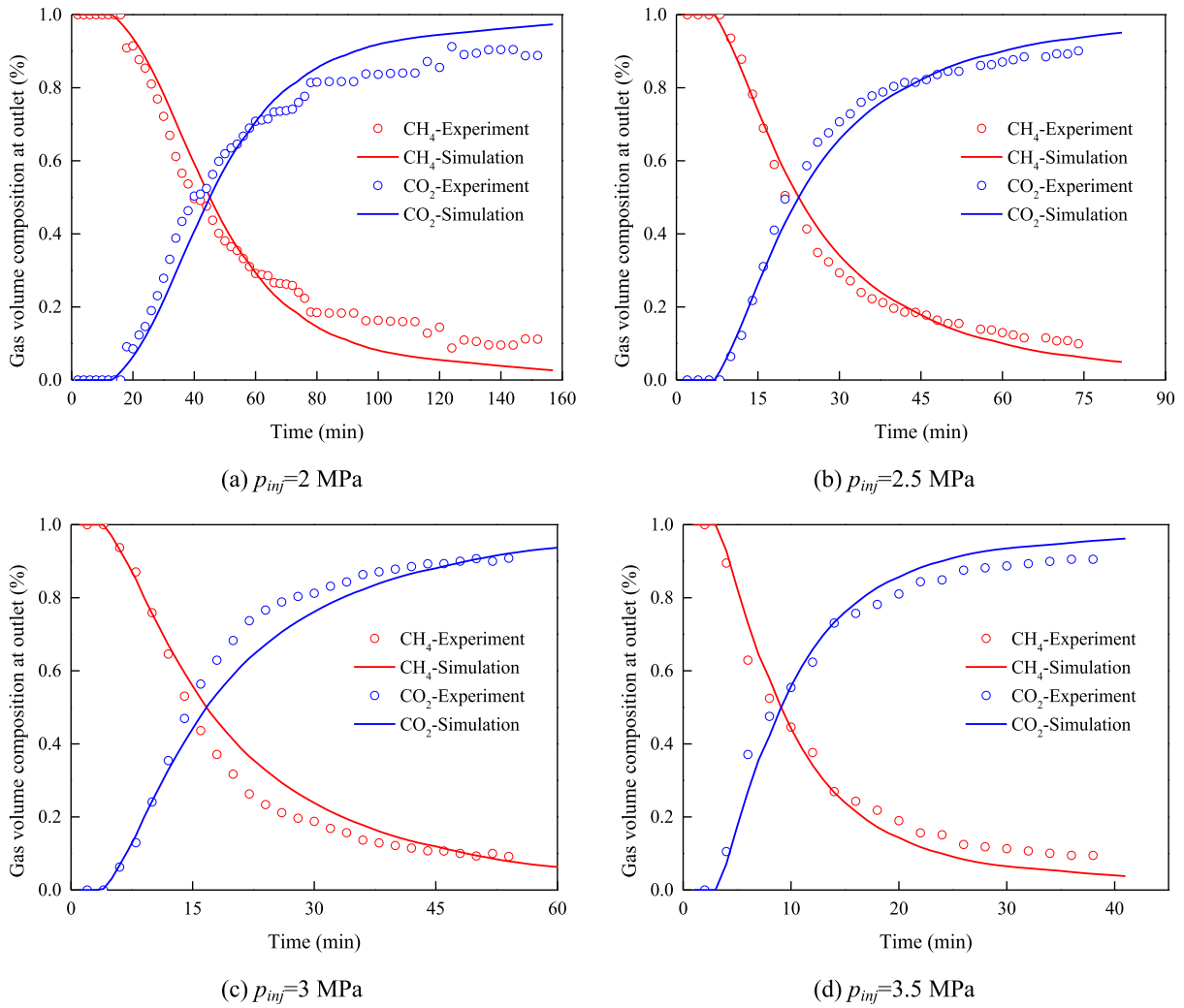(d) p_{inj}=3.5 MPa

Fig. 5. Volume composition histories of CH_4 and CO_2 at output for various relative injection pressures.
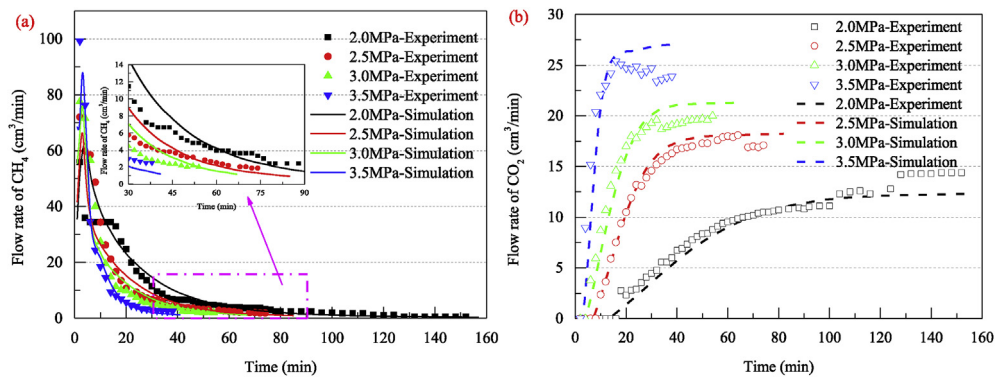

Fig. 6. Comparison between simulated and experimental flow rates: (a) CH_4 flow rate, (b) CO_2 flow rate.

15.6%, and those of CO_2 flow rate are 11.7, 3.3, 9.9 and 13.2%, respectively. A slight deviation of the CO_2 flow rate is apparent between observations and model results in the high rate stage, but the modelling and experimental results are generally in good agreement.

4. Numerical simulation on CO_2 sequestration and enhanced CBM recovery

4.1. Simulation case and conditions

Qinshui Basin, one of the earliest and most commercially viable

areas for CBM exploration and development in China. With an estimated methane reserve about $3.28 \times 10^{12}\,m^3$ at standard conditions, it is located in the southeast of Shanxi Province, ~210 km south of Taiyuan, and ~60 km northwest of Jincheng. The primary target zone is coal seam #3 in the Shanxi Formation of uniform thickness (5−6 m), high permeability (0.01−10 mD), high gas content (8.27−21.54 m^3/t) and shallow burial depth (~600 m). A pilot CO_2-ECBM recovery demonstration project began in 2002 [13] with wells in a traditional five-spot pattern (Fig. 7a) [51,52], comprising a central injection well surrounded by four production wells. We simulate the upper right (NE) quadrant (~1/4) of this near-regular five-spot pattern as a 150 m × 150 m × 5 m block as shown in Fig. 7b. Actually, the simulated distance between adjacent production wells is 300 m. The injection and production wells (0.1 m in diameter) are arranged at the lower left and upper right corners of the geometric model, respectively.

The basal boundary is for zero deformation with slip conditions applied to the surrounding boundaries and overburden loading on the upper boundary. For the fluid flow (CH_4, CO_2, and water), a constant pressure of 0.15 MPa is applied to the production well and 8 MPa to the injection well (no gas flow to the injection well in the primary recovery). An injection temperature of 323 K is applied to the injection well with all the other external boundaries insulated for both fluid and heat flow.

The initial reservoir pressure is 5.24 MPa, initial reservoir temperature is 305.5 K, initial water saturation is 0.82 and initial permeability is $5.14 \times 10^{-16}\,m^2$. Other parameters used in the simulations are listed in Table 2 as recovered from the public domain [3,48,51,52,69,70]. The solution grid comprises 4860 elements and 67 435° of freedom using tetrahedral elements and with simulation extended over 5000 days (~14 years). The reference section (Line A-B) and three points (P1, P2, P3) are used to report the evolution of reservoir parameters.

According to Eq. (12) and the parameters in Table 2, we plot the relative permeability in Fig. 8. The gas relative permeability is relatively low when the water saturation is larger than 0.6, indicating that the gas is transported slowly in the water rich reservoir.

Fig. 9 shows the change in adsorbed gas content in the coal seam with reservoir temperature and gas pressure. The adsorbed gas content of CO_2 is significantly larger than that of CH_4, implying that CO_2 has a stronger adsorption capacity when competing with CH_4. With an increase in reservoir temperature, the adsorbed gas content of both CO_2 and CH_4 decrease. For example, the gas contents of CO_2 under a gas pressure of 5.24 MPa are 0.0483, 0.0352, and 0.0259 m^3/kg at temperatures of 285.5, 305.5, and 325.5 K,

Fig. 8. Relative permeability curves for gas and water.
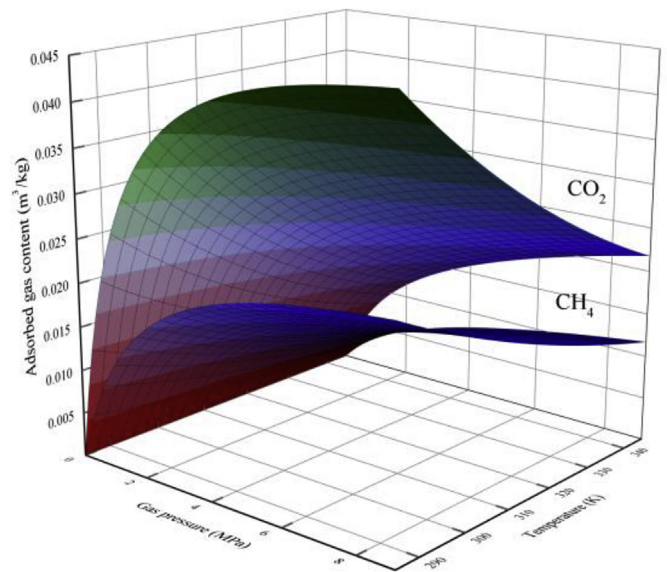
Fig. 9. Variation of adsorbed gas content of CO_2 and CH_4 relative to gas pressure and temperature.

respectively. While, the corresponding gas contents of CH_4 are 0.0248, 0.0183, and 0.0134 m^3/kg, respectively. This indicates the
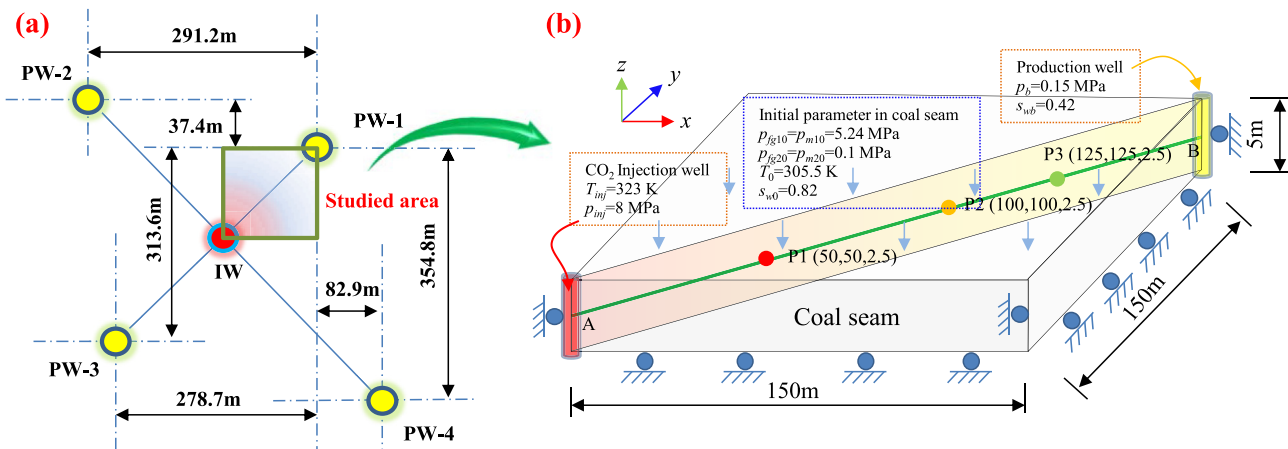

Fig. 7. (a) Configuration of five-spot pattern well for CO_2-ECBM pilot test and (b) geometric model for CO_2-ECBM simulation.
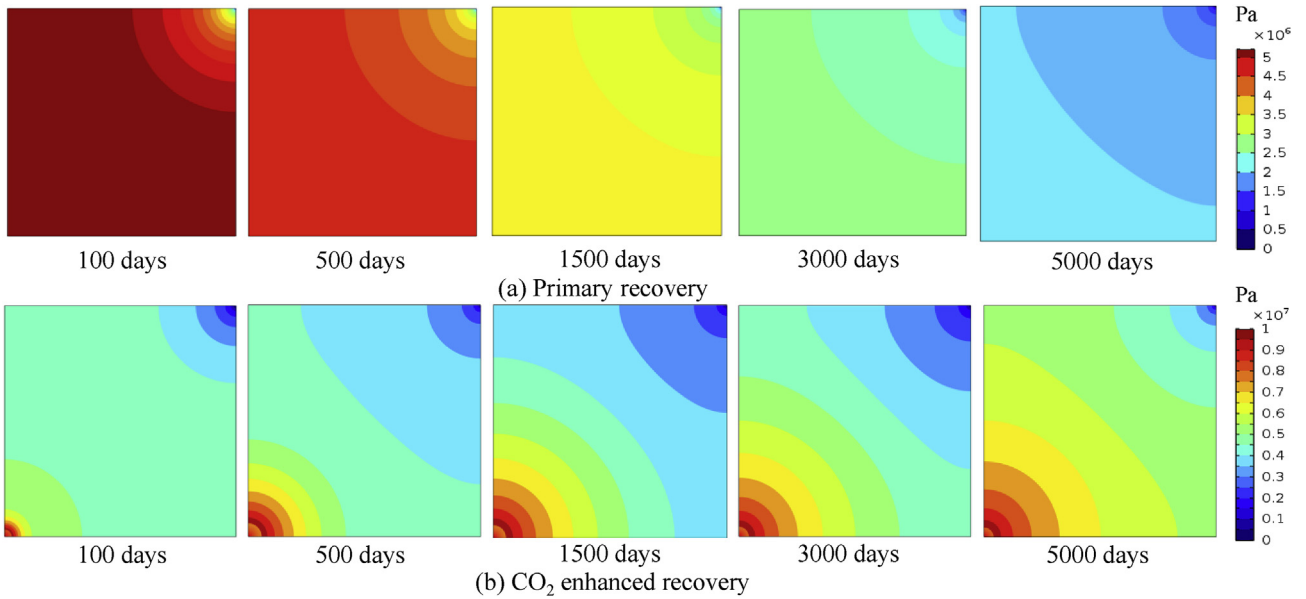
Fig. 10. Reservoir pressure in coal seam during primary recovery and CO_2 enhanced recovery.
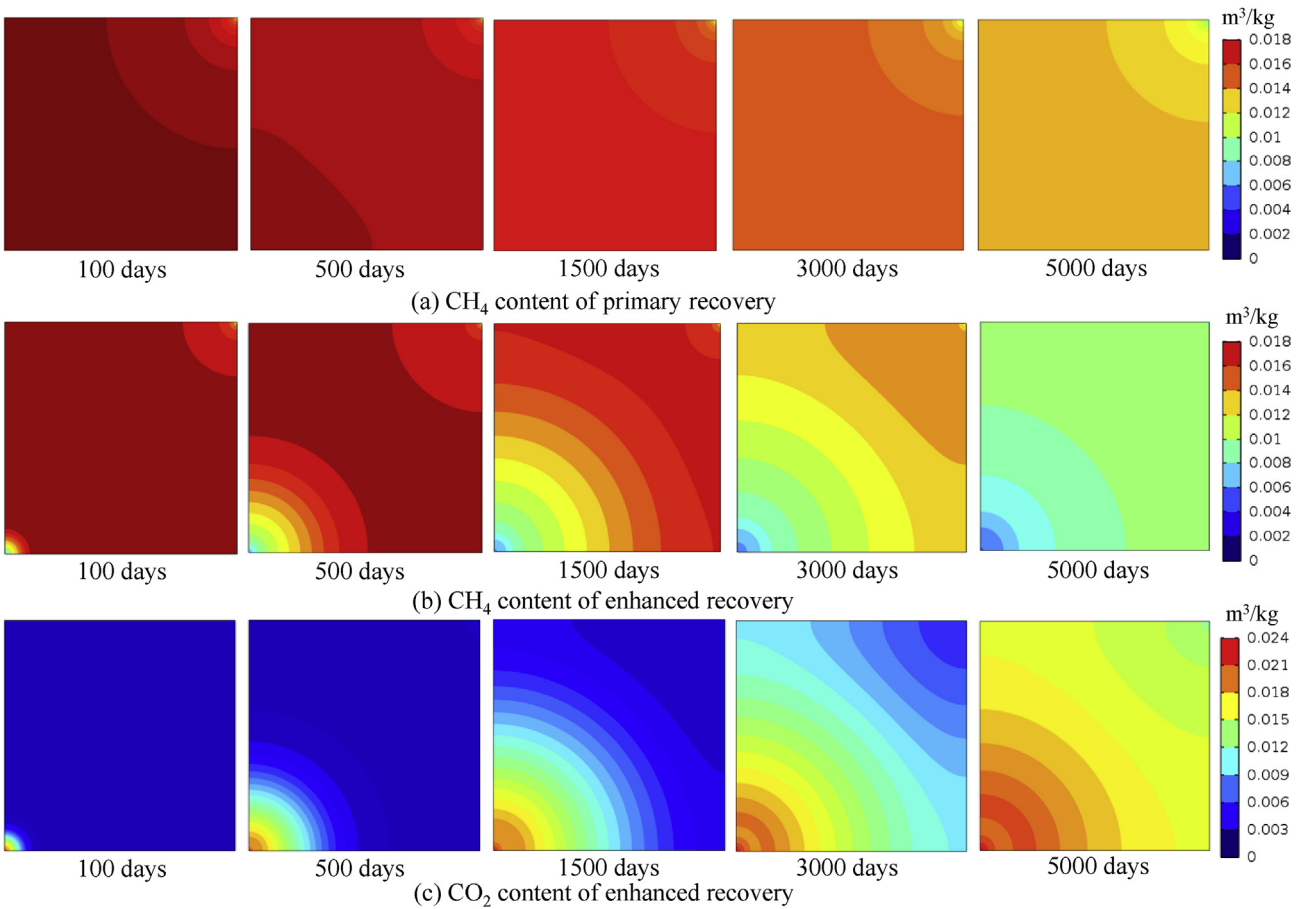

Fig. 11. Distribution of gas content in the coal seam during primary recovery and CO_2 enhanced recovery.

significant impact of temperature on gas content in coal reservoirs and cannot be ignored.

4.2. Results of numerical simulations

4.2.1. Distribution of reservoir pressure

We simulate the process of both primary CBM recovery and CO_2

enhanced CBM recovery, for comparison. The reservoir pressure is defined by the gas pressure in the fractures, which is equal to the gas pressure of CH_4 in the fractures for primary recovery and the sum of gas pressures of CH_4 and CO_2 in the fractures for enhanced recovery. The distribution of reservoir pressure is presented in Fig. 10. For primary recovery without CO_2 gas injection, the reservoir pressure continuously drops until reaching the bottom pressure in the production well (Fig. 10a). After production for 5000 days, the reservoir pressure in the entire coal seam has decreased to <2.5 MPa. In the case of enhanced recovery with CO_2 injection, the reservoir pressure near the injection well increases rapidly while the reservoir pressure at the production well first gradually decreases, then rebounds (Fig. 10b). Due to the stronger adsorption capacity, injected CO_2 will displace absorbed CH_4 within matrix, accelerating CH_4 desorption, then diffusing into the fractures to increase CH_4 pressure in fractures [71,72].

4.2.2. Distribution of gas content

Fig. 11 shows the variation of gas content in the coal reservoir for both primary and enhanced recovery. For primary recovery, the gas content around the production well gradually decreases and expands to fill the entire reservoir (Fig. 11a). For enhanced recovery the CH_4 content decreases at both production well and injection well with the duration of injection. The competitive adsorption effect of CO_2 causes the CH_4 content near the injection well to drop and the desorbed CH_4 increases the gas pressure within the fracture to drive CH_4 towards the production well (Fig. 11b). Compared with primary recovery, the CH_4 content of enhanced recovery first increases slightly and then sharply decreases. In Fig. 11c, the gas content of CO_2 in the coal seam increases with production time, particularly near the injection well.

4.2.3. Reservoir temperature

The reservoir temperature is closely related to the heat transfer in the coal seam. Fig. 12 shows the reservoir temperature along reference section A-B during both primary recovery and CO_2 enhanced recovery. For primary recovery, the temperature within the coal reservoir gradually decreases with production time - from an initial temperature of 305.5 K to the final temperature of ~302.5 K at 5000 days (Fig. 12a). The gas desorption consumes energy, causing a drop in reservoir temperature. Therefore, the temperature near the production well decreases faster than that in the interior of the coal reservoir. In Fig. 12b, the reservoir temperature

during CO_2 enhanced recovery increases with production time with the variation being more complex. The reservoir temperature is the competitive result of the cooling induced by CH_4 desorption, and the heating by the injection temperature and CO_2 adsorption. Close to the injection well, the injected high temperature flux, together with the energy released by adsorption of CO_2, strengthens the heat transfer within the reservoir. Hence, warming dominates near the injection well, leading to a rapid temperature increase, from 305.5 K to 323.15 K. Proximal to the production well, the reservoir temperature is greatly influenced by both CH_4 desorption and CO_2 adsorption. Before the arrival of the injected CO_2 (~1000 days), the reservoir temperature decreases slightly with CH_4 desorption. Following this, CO_2 adsorption dominates to elevate reservoir temperature.

4.2.4. Permeability ratio

Fig. 13 illustrates the permeability ratio at reference points P1 (50, 50, 2.5), P2 (100, 100, 2.5), and P3 (125, 125, 2.5). In Fig. 13a, the permeability at the primary recovery points P1, P2 and P3 first decreases due to the depletion of reservoir pressure, and then rebounds due to the desorption of CH_4. The minimum permeability ratio at point P1 is ~0.99 at 800 days, and this reaches a maximum value of ~1.055 at 5000 days. The permeability closer to the production well exhibits an earlier decrease and rebound leading to a more significant impact on gas production. In Fig. 13b, the permeability variation due to the enhanced recovery (utilizing CO_2) becomes more complex. CH_4 desorption and the induced cooling will increase the fracture permeability, with this countered by the adsorption of CO_2 which raises temperature and decreases the permeability. The resulting permeability is the combined result of these two opposing effects. Near the production well (P2, P3), the permeability first decreases due to the increase of effective stress (reservoir pressure decrease), but before it rebounds to the initial value, the arrival of CO_2 impacts the permeability. As a result, the permeability ratio continuously decreases to a very low magnitude (~0.713 for P3, ~0.7 for P2) at 5000 days. Near the injection well (P1), due to the low relative gas permeability at initiation, the CH_4 pressure drops slightly and CO_2 pressure increases slowly. Therefore, the permeability remains stable over the first 300 days of production (dewatering stage). After that, the relative gas permeability at P1 increases, leading to a rapid increase of the mass of injected CO_2. The permeability ratio decreases dramatically over time, from 0.997 (300 days) to 0.659 (5000 days).
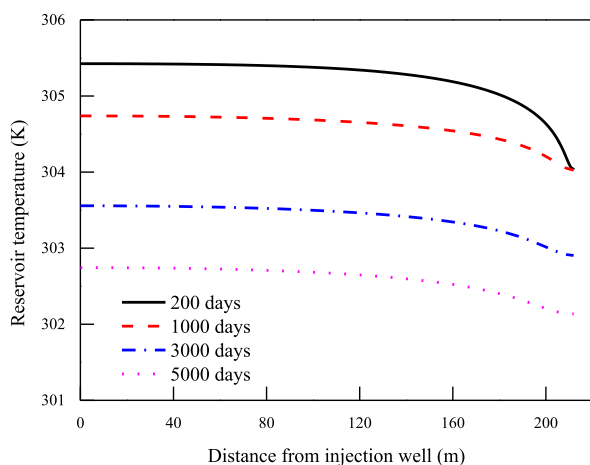
(a) Primary recovery
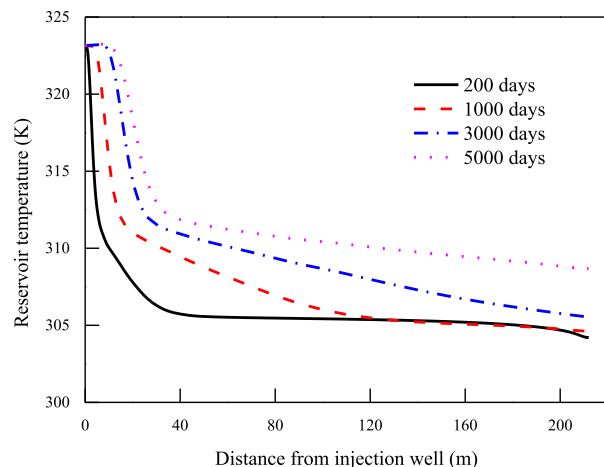
(b) Enhanced recovery

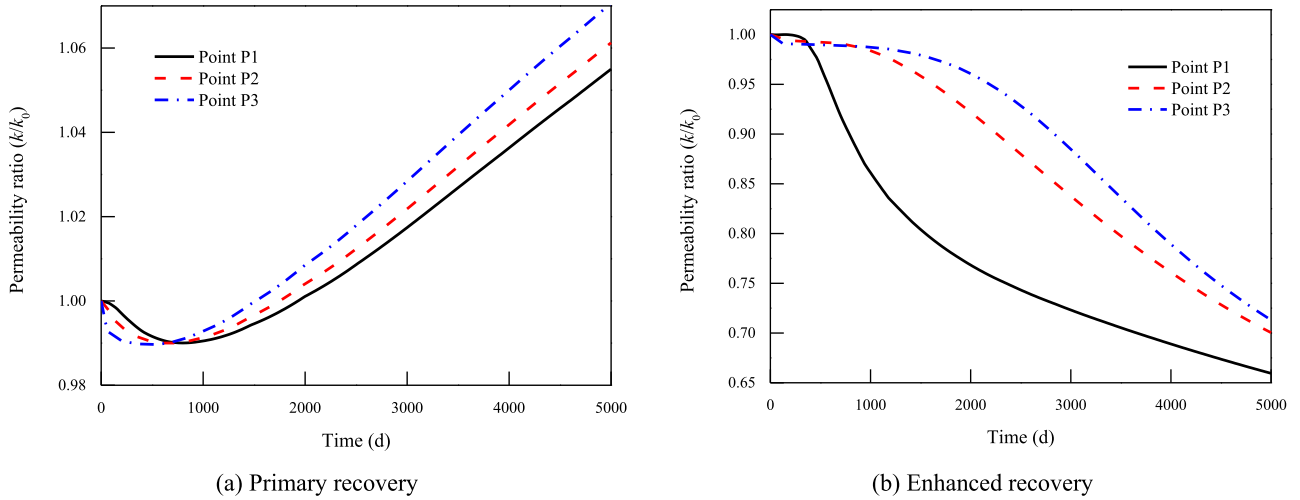**Fig. 12.** Reservoir temperature along the reference section A–B relative to production time.

(a) Primary recovery

(b) Enhanced recovery

Fig. 13. Evolution of permeability ratio at the three reference points (P1, P2, P3) within the coal reservoir.

4.2.5. CH_4 production and CO_2 storage

Fig. 14 presents the gas production during primary and enhanced recovery. As shown in Fig. 14a, both CH_4 production rate and CO_2 recovery rate first increase in early time then reduce at late time. The peak production rate for primary recovery is 1670.1 m^3/d (420 days) and for enhanced recovery is 1919.3 m^3/d (780 days). Compared with primary recovery, the peak production rate for enhanced recovery is both elevated and delayed. In the dewatering stage, a similar variation of the production rate is found between primary and enhanced recovery. However, after this stage, the injected CO_2 within the coal seam dominates response *via* competitive adsorption - this promotes the transport of CH_4 to the production well, finally raising the CH_4 production rate. The extended duration of dewatering, combined with the low initial gas relative permeability proximal to the injection well, delays the peak injection rate of CO_2. CO_2 breakthrough appears at 1620 days when the CO_2 recovery rate begins to increase, ultimately reaching 249.4 m^3/d (5000 days) at a CO_2 concentration of ~20.28% in the produced gas flow. Fig. 14b shows the variation of cumulative CH_4 production and CO_2 storage over time. At 5000 days, the cumulative CH_4 production for primary recovery is 5.1 million m^3, and the

cumulative CH_4 production for enhanced recovery is 7.38 million m^3 - an increase of 44.6%. The recovery ratio is defined as the proportion of the cumulative CH_4 production to the initial amount of CH_4 in the coal reservoir. For primary recovery, the recovery ratios at 500, 1500, 3000, and 5000 days are 6.2%, 18.8%, 32.1% and 43.8%, with the corresponding values for enhanced recovery of 6.5%, 22.6%, 43.1% and 63.3%, respectively. The injection of CO_2 effectively increases the recovery ratio. Meanwhile, we define the enhancement factor as the proportion of recovery ratio of enhanced recovery to that of primary recovery. Accordingly, the enhancement factor due to ECBM is 1.05, 1.2, 1.35, and 1.45 respectively at the incremented times. The cumulative CO_2 storage approaches 12.84 million m^3 at 5000 days, indicating a significant CO_2 storage capacity and the potential viability for CO_2 sequestration within the coal seam.

5. Discussion on coupling relations and sensitive factors

5.1. Coupling relations

In order to gain insight into the key THMC process that control
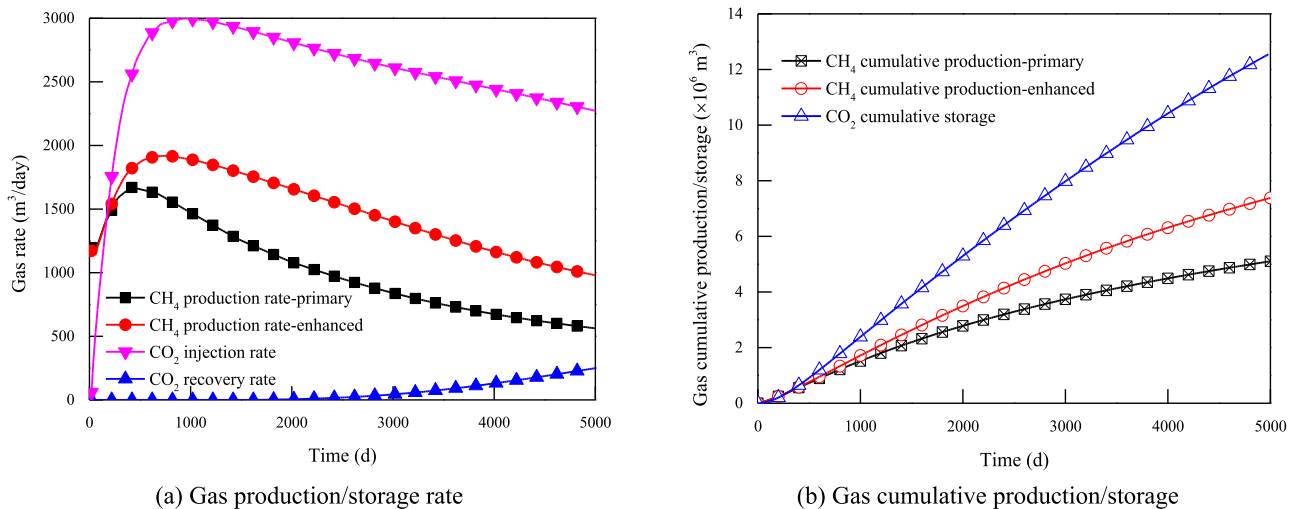

(a) Gas production/storage rate

(b) Gas cumulative production/storage

Fig. 14. Gas production and storage during primary and enhanced recovery.

Table 3
Simulation schedules of different coupled models.

	Models	Coupling relationships (see Fig. 3)	Remark
Scenario I	__MC model	Relations (1)–(8)	No heat, no water
Scenario II	T_MC model	Relations (1)–(8), and (15)–(18)	With heat, no water
Scenario III	_HMC model	Relations (1)–(12)	No heat, with water
Scenario IV	THMC model	Relations (1)–(18)	With heat and water

response, we compare the response of four separate models (Table 3) with different coupling relationships. We represent these couplings, either incorporating or absent heat transfer (T) and/or two phase flow (water transport (H)) and gauge their impact with respect to the resulting CO_2-ECBM recovery. Scenario I (no heat, no water − __MC model) incorporates the interactions of gas migration, competitive sorption (C) and coal deformation (M) but ignores the impacts of water migration and heat transfer. Scenario II (heat, no water − T_MC model) incorporates heat transfer on the basis of scenario I but ignores water migration. Scenario III (water, no heat − _HMC model) incorporates water migration but ignores heat transfer. And, Scenario IV (heat, water − THMC model) incorporates all coupling relations, including water and gas migration, competitive sorption, coal deformation, and heat transfer. The resulting evolution of gas content, permeability ratio, CH_4 production, and CO_2 storage are compared.

5.1.1. Gas content

Fig. 15 shows gas content along section A-B. As illustrated in Fig. 15a, the CH_4 content decreases gradually over time. Due to the displacement effect of CO_2 and thermal effect on gas sorption, the CH_4 content near the injection well decreases more rapidly than at the interior. The CH_4 content along section A-B shows a "saddle" shape. The CH_4 content of the T_MC model decreases most rapidly, followed by the __MC, THMC and _HMC models, respectively. However, an abnormal situation occurs around the CO_2 injection well - the CH_4 content of models incorporating heat transfer reduce more drastically. The gas desorbed by warming is transported to the inner region to compensate for the reduction in CH_4 content. Fig. 15b presents the change of CO_2 content along section A-B where the CO_2 content increases with injection time. With a low initial gas relative permeability, the CO_2 content of the models

(_HMC, THMC) considering water transport increases much faster than that of models where dewatering is ignored (__MC, T_MC). The high temperature of the injected CO_2 reinforces heat transfer within the coal seam, elevating reservoir temperature. Hence, the CO_2 content of the models considering heat transfer (T_MC, THMC) increases more slowly than that of models where it is ignored (__MC, _HMC).

5.1.2. Reservoir permeability

Fig. 16 shows the permeability evolution along section A-B and point P2 for the different coupled models. In Fig. 16a, the permeability decreases rapidly over time. The permeabilities along section A-B are in the order: _HMC model > THMC model > __MC model > T_MC model. The permeability of models considering water migration (_HMC, THMC) reduces more slowly than that of models where it is ignored (__MC, T_MC). Conversely, the permeability of models considering heat transfer (T_MC, THMC) decreases more rapidly than that in models where it is ignored (__MC, _HMC), especially in areas recording significant change in reservoir temperature. Due to the impact of matrix shrinkage induced by gas desorption, a rapid increase in permeability is observed proximal to the production well. In Fig. 16b, before the arrival of the CO_2 front, the permeability at point P2 of all four models differs only slightly. Without the participation of CO_2, the evolution of permeability is the competitive result of the matrix shrinkage induced by CH_4 desorption and the compaction by the increasing effective stress (gas pressure depletion) - the permeability first decreases, then increases. This phenomenon is also apparent in Fig. 13. The models considering water migration (_HMC, THMC) show a delayed change in permeability. After the arrival of the CO_2 front, the matrix swelling induced by CO_2 adsorption dominates the response, leading to a sharp decrease in permeability for all four models.

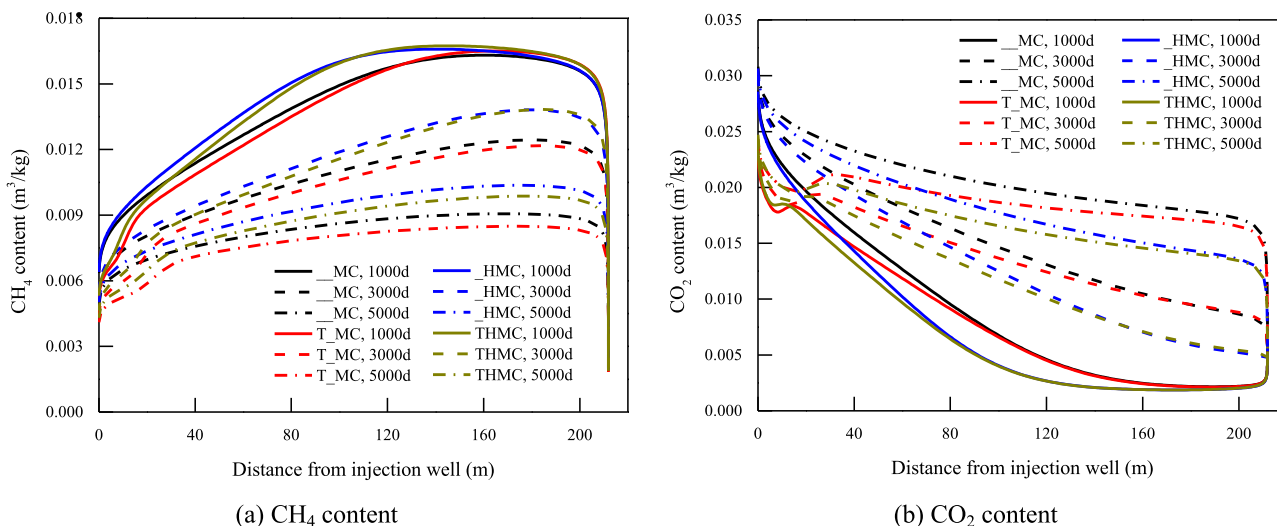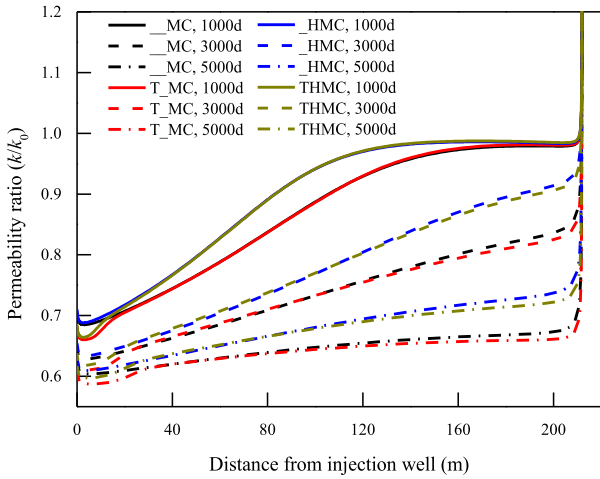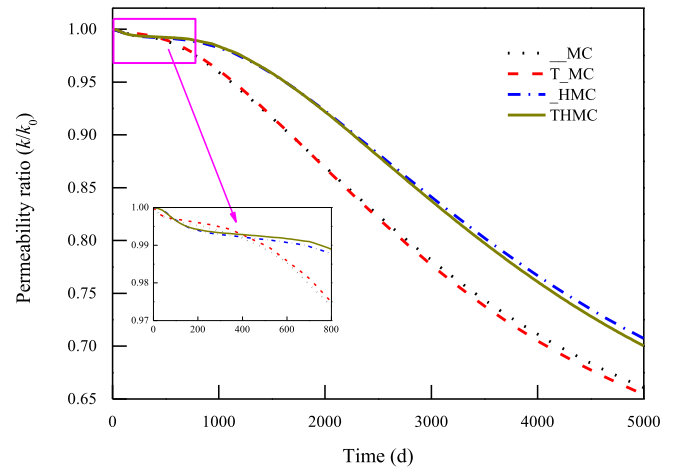(a) CH_4 content

(b) CO_2 content

Fig. 15. Variation of gas content along the reference section A-B for different coupled models.
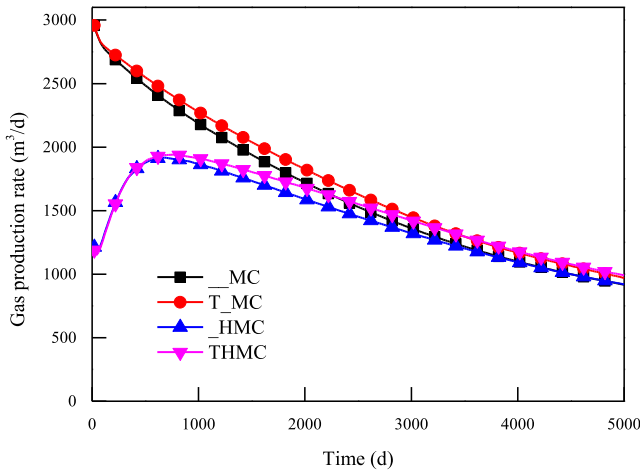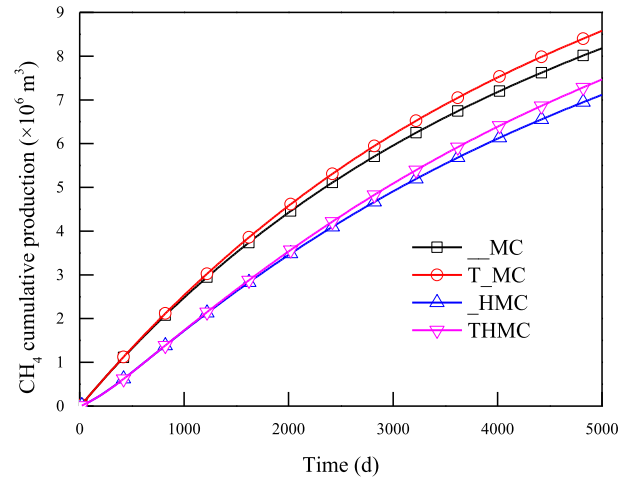
(a) Permeability ratio along reference section A-B

(b) Permeability ratio at reference point P2

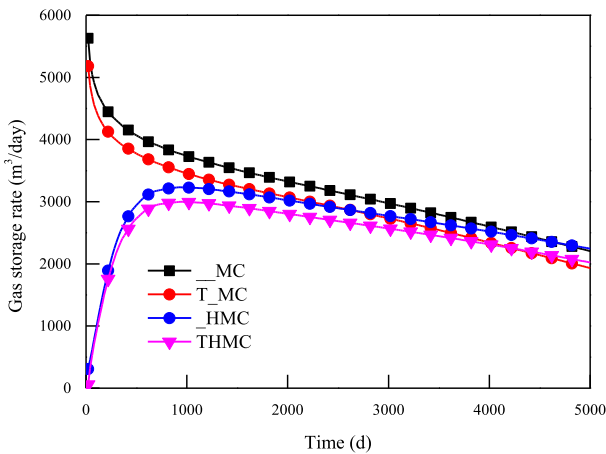**Fig. 16.** Evolution of reservoir permeability for different coupled models.
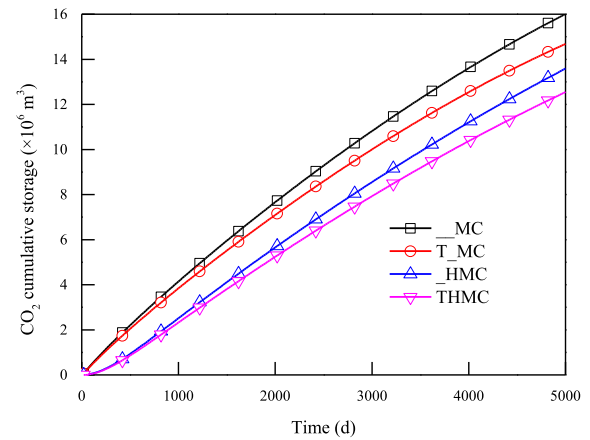

(a) CH$_4$ production rate

(b) CH$_4$ cumulative production

Fig. 17. CH$_4$ production for different coupled models.

(a) CO$_2$ storage rate

(b) CO$_2$ cumulative storage

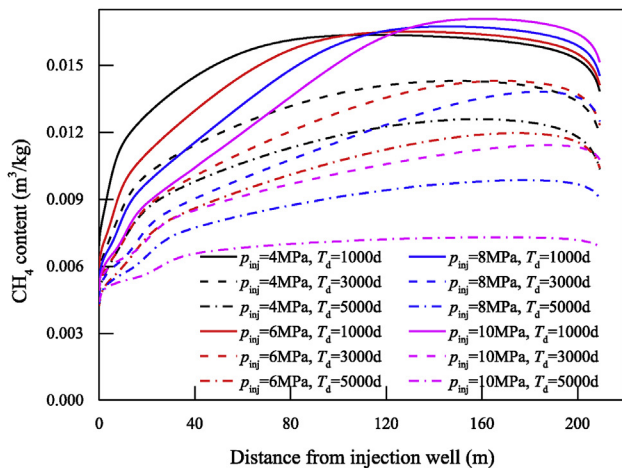**Fig. 18.** CO$_2$ storage for different coupled models.

5.1.3. CH₄ production and CO₂ storage

As shown in Fig. 17a, the CH$_4$ production rate of the __MC and T_MC models decreases with production time, while the CH$_4$ production rate of the _HMC and THMC models first increases to peaks of 1917.6 m^3/d (~680 days) and 1941.4 m^3/d (~780 days), respectively, before reducing. This peak results from the relatively low initial gas relative permeability during the dewatering stage. The presence of water blocks the migration of CH$_4$ from the reservoir resulting in an increasing process of gas production rate, as observed in situ [21]. The adsorption of CO$_2$ and the associated high heat flux elevates the reservoir temperature and further enhances CH$_4$ desorption. From this perspective, the gas production rate of models considering heat transfer is greater than that of models where thermal impacts are ignored. In Fig. 17b, the cumulative CH$_4$ production in the order of highest to lowest is: T_MC model > __MC

model > THMC model > _HMC model. The cumulative production of CH$_4$ over 5000 days for these four models (__MC, T_MC, _HMC and THMC) are 8.18, 8.58, 7.11, and 7.47 million m^3, with corresponding recovery ratios of 70.2%, 73.6%, 61%, and 63.3%, and with enhancement factors of 1.6, 1.68, 1.39 and 1.46, respectively. Therefore, ignoring the impacts of water migration clearly overestimates gas production, and ignoring the impacts of heat transfer underestimates gas production.
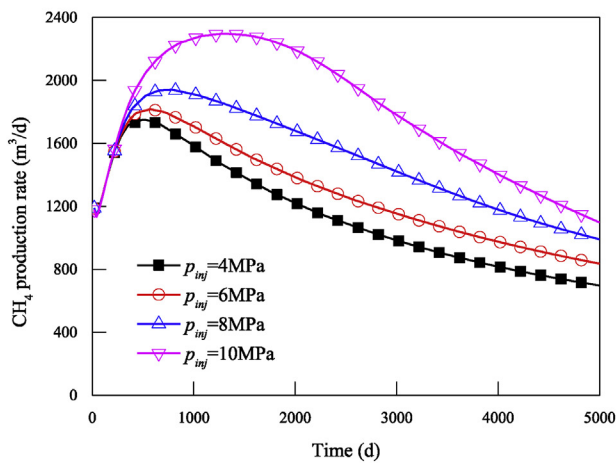
Fig. 18 compares the resulting volume of CO$_2$ sequestered for these four models. In Fig. 18a, similar with CH$_4$ production rate, the CO$_2$ storage rates for the __MC and T_MC models decrease with the progress of injection, and the CO$_2$ storage rates for the _HMC and THMC models first increase to peaks of 3232.3 m^3/d (~920 d) and 2998.7 (~940 d), respectively, before decreasing. The average storage rate for models considering water migration (_HMC, T_MC) is smaller than that of models where it is ignored (__MC, T_MC). The warming of the reservoir inhibits CO$_2$ adsorption and promotes CH$_4$ desorption. Hence, the impact of thermal effects on CH$_4$ production is opposite its impact on CO$_2$ storage - the models ignoring heat transfer (__MC, _HMC) have a larger CO$_2$ storage rate than the models considering heat transfer (T_MC, THMC). Cumulative CO$_2$ storage increases with injection time (Fig. 18b) with CO$_2$ cumulative storage increasing in the order: __MC model > T_MC model > _HMC model > THMC model. The corresponding CO$_2$

Table 4
Simulation schedules of sensitive factors.

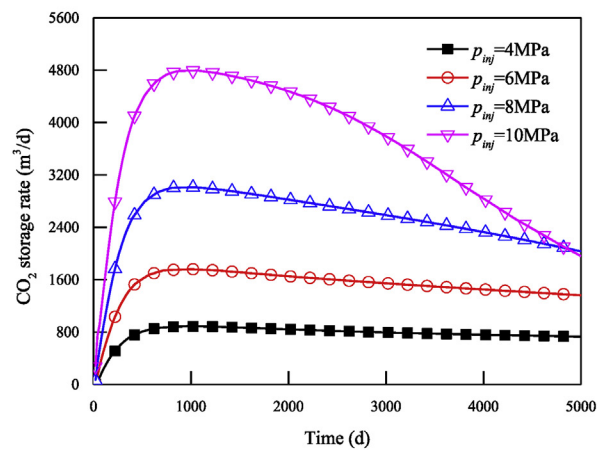| Parameter	Basic value	Variation	Remark
Injection pressure (p_{inj})	8.0	4.0, 6.0, 8.0, 10.0	MPa
Injection temperature (T_{inj})	323	283, 303, 323, 343	K
Initial water saturation (s_{w0})	0.8	0.5, 0.6, 0.7, 0.8	–
Initial permeability (k_0)	5.14	1.14, 3.14, 5.14, 7.14	10^{-16} m^2

(a) CH₄ content on reference line A-B
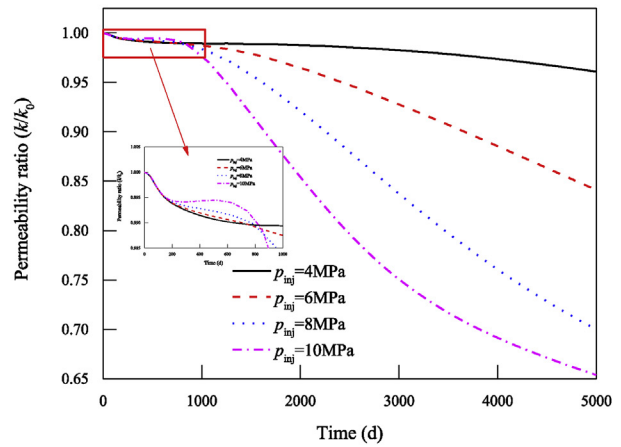
(b) Permeability at reference point P2

(c) CH₄ production rate

(d) CO₂ storage rate

Fig. 19. Variation of recovery, storage and permeability relative to different injection pressures.

cumulative storage over 5000 days is 16.01, 14.68, 13.59, 12.54 million m^3, respectively. Taking the proposed THMC model as a reference, the other three models (__MC, T_MC, _HMC) will overestimate the cumulative storage with a deviation of 27.6%, 17%, and 8.3%, respectively.

5.2. System sensitivity

We discuss the effects of key factors influencing CH_4 production rate, CO_2 storage rate, CH_4 content, and permeability in coalbed reservoirs. These factors include the injection pressure (p_{inj}), injection temperature (T_{inj}), initial water saturation (s_{w0}), and initial permeability (k_0). This method of controlling variables is used to explore the sensitivity of factors to the simulated results of CO_2-ECBM recovery. The simulation schedules for these various sensitive factors are listed in Table 4.

5.2.1. Injection pressure

Fig. 19 shows the variation of recovery, storage and permeability during CO_2-ECBM recovery for different injection pressures. CH_4 content is controlled by CH_4 desorption and migration. This, in turn, depends on drainage activity driven by suction pressure and by CO_2 displacement prompted by injection pressure and temperature. The CH_4 content along section A-B decreases with time, especially near the production and injection wells (Fig. 19a). In general, higher

injection pressure results in greater reduction of CH_4 content than a lower injection pressure, despite permeability under high injection pressure decreasing more rapidly (Fig. 19b). After injection for 5000 days, the permeability ratio for an injection pressure of 10 MPa decreases to ~0.654. In Fig. 19c and d, the CH_4 production rate and CO_2 storage rate both increase with injection pressure. The peak production rates for injection pressures of 4, 6, 8, and 10 MPa are 1752, 1816, 1941, and 2297 m^3/d at 500, 580, 780, and 1280 days respectively - illustrating that higher injection pressure results in a greater and successively more delayed peak rate. The corresponding peak storage rates are 889, 1761, 3011, and 4791 m^3/d, respectively. The increase of injection pressure increases the pressure gradient between injection well and coal reservoir, which greatly promotes CO_2 migration, and thus the displacement effect. As a result, the CH_4 production rate and CO_2 injection rate increase.

5.2.2. Injection temperature

Fig. 20 shows the variation of recovery, storage and permeability during CO_2-ECBM recovery for different injection temperatures. Apparent in Fig. 20a is that a notable region near the injection well develops where CH_4 content differs from the remainder of the reservoir. In this region, thermal effects on gas sorption dominate the response. Low temperature CO_2 flow enhances the sorption of CH_4 and CO_2. The increased gradient of reservoir pressure resulting from the rapid sorption of CO_2 promotes the transport of CO_2 and

(a) CH_4 content along the section A-B

(b) Permeability at point P2

(c) CH_4 production rate
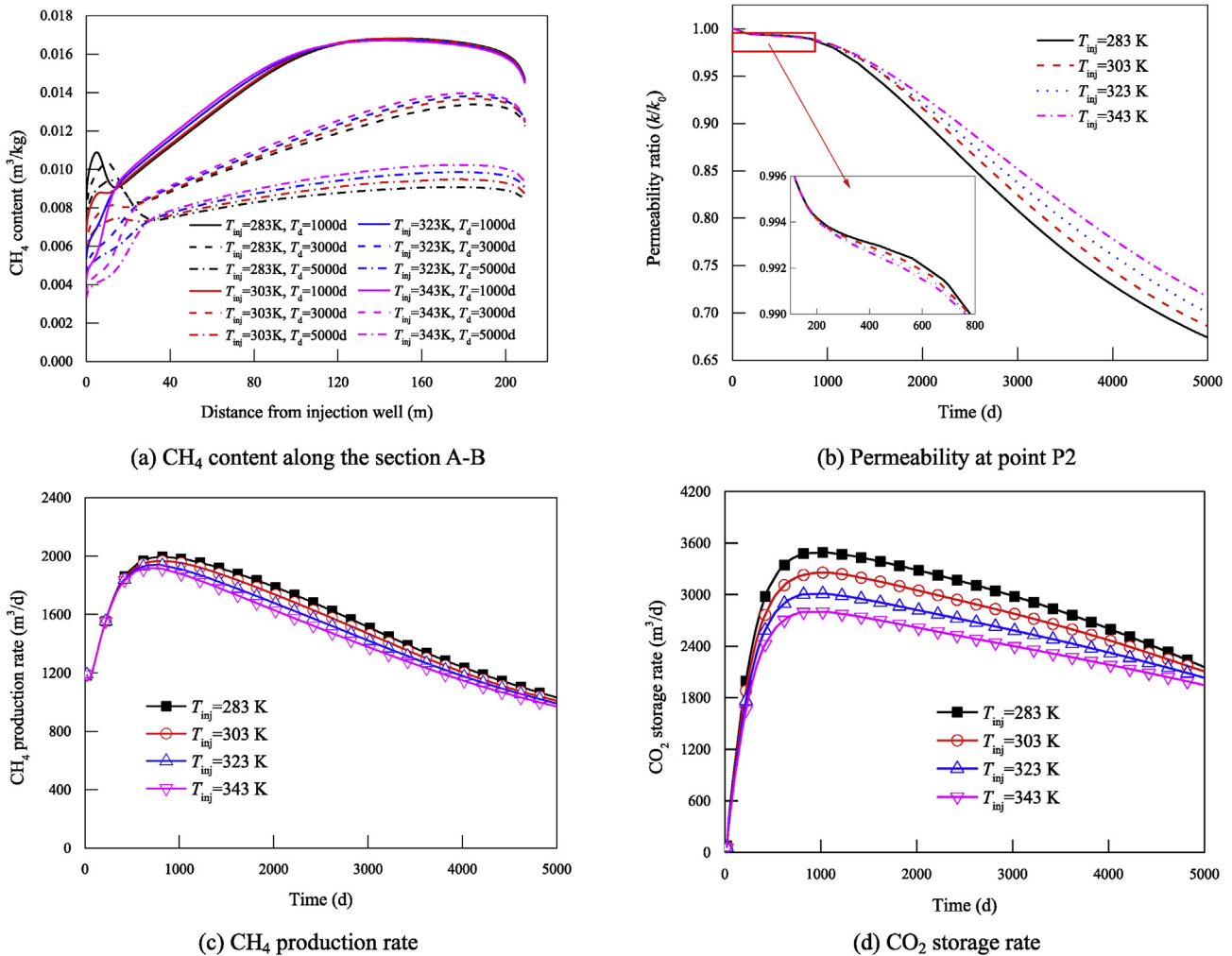
(d) CO_2 storage rate

Fig. 20. Variation of recovery, storage and permeability relative to different injection temperatures.

results in early breakthrough at the production well. However, remote from the injection well the adsorption rate of CH_4 decreases more rapidly due to the reduced thermal effect on gas sorption. Permeability at low injection temperatures decreases more rapidly (Fig. 20b). After production for 5000 days, the permeability ratio for the injection temperature of 283 K drops to ~0.674. As apparent in Fig. 20c and d, the CH_4 production rate and CO_2 storage rate both decrease with increasing injection temperature. The peak production rates for injection at 283, 303, 323 and 343 K are 1998, 1967, 1941 and 1919 m^3/d, respectively. The warming of the reservoir reduces the adsorption capacity of CO_2, and thus the displacement effect. This illustrates that lower injection temperatures result in improved cumulative production via increases in incremental injection rates.

5.2.3. Initial water saturation

High initial water saturation corresponds to only a small reduction in CH_4 content (Fig. 21a). In reservoirs with high initial water saturations, gas production is preceded by a relatively long period of dewatering. Initial low gas phase relative permeability results in only a small reduction in CH_4 content. Higher initial water saturation leads to a slower decrease in reservoir permeability (Fig. 21b). At 5000 days, the permeability ratios for initial water saturations of 0.5, 0.6, 0.7, and 0.8 decrease to 0.687, 0.692, 0.696

and 0.701, respectively. Water production increases with initial water saturation, but both CH_4 production and CO_2 storage rates decrease, as apparent in Fig. 21c and d. The corresponding peak production rates are 2399, 2065, 1987, and 1941 m^3/d at 0, 420, 660, and 780 days, respectively. This indicates that a higher initial water saturation results in a reduced and more delayed peak production rate. In addition, late stage gas production and storage rates decrease more slowly, for higher initial water saturation, due to a slower drop in reservoir pressure and a larger pressure gradient between production well and reservoir. Overall, water blocks the migration of the binary gas, and delays the arrival of both peak production and injection rates, finally reducing the capacities for CH_4 production and CO_2 storage.

5.2.4. Initial coalbed permeability

Coalbed permeability determines the rapidity of gas migration from fractures to the production well during CO_2-ECBM recovery. A higher initial permeability greatly promotes mass transport, leading to greater reduction in CH_4 content (Fig. 22a). When the initial permeability is relatively high, the reservoir permeability decreases more rapidly (Fig. 22b). For example, the permeability ratio at point P2 for an initial permeability of 7.14×10^{-16} m^2 continuously decreases to a ratio of ~0.631. Although the permeability ratio decreases drastically with the initial permeability, the absolute
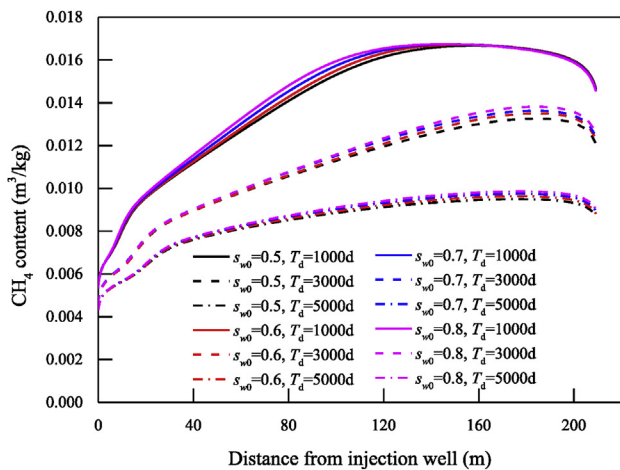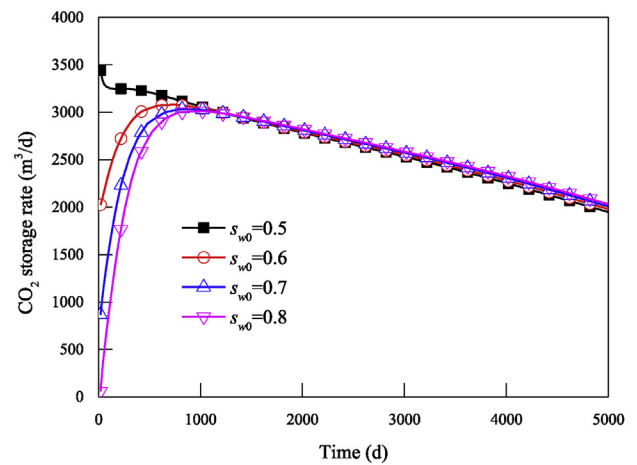

(a) CH_4 content along the section A-B
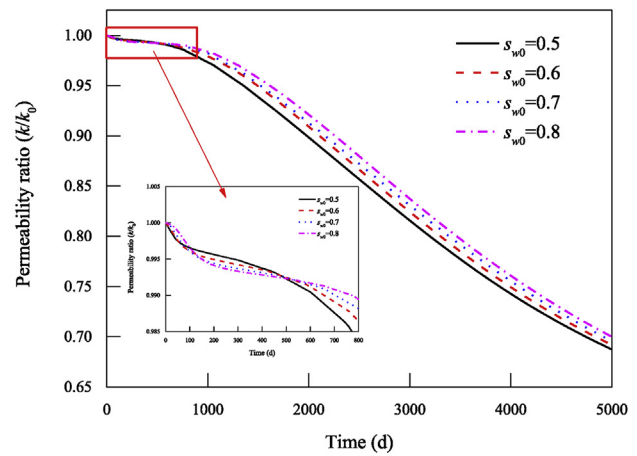
(b) Permeability at point P2
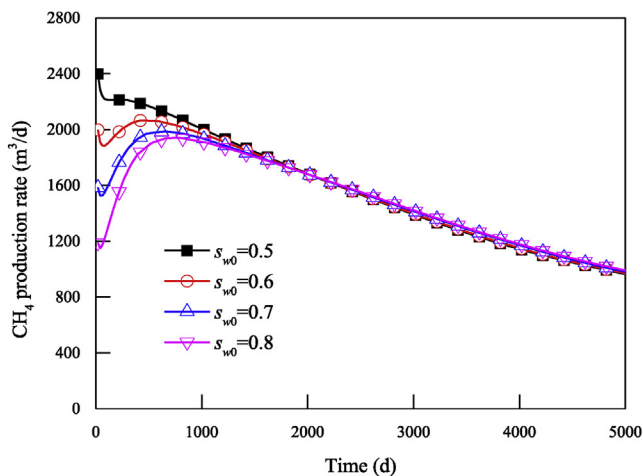
(c) CH_4 production rate

(d) CO_2 storage rate

Fig. 21. Variation of recovery, storage and permeability relative to different initial water saturations.

(a) CH₄ content along the section A-B

(b) Permeability at point P2
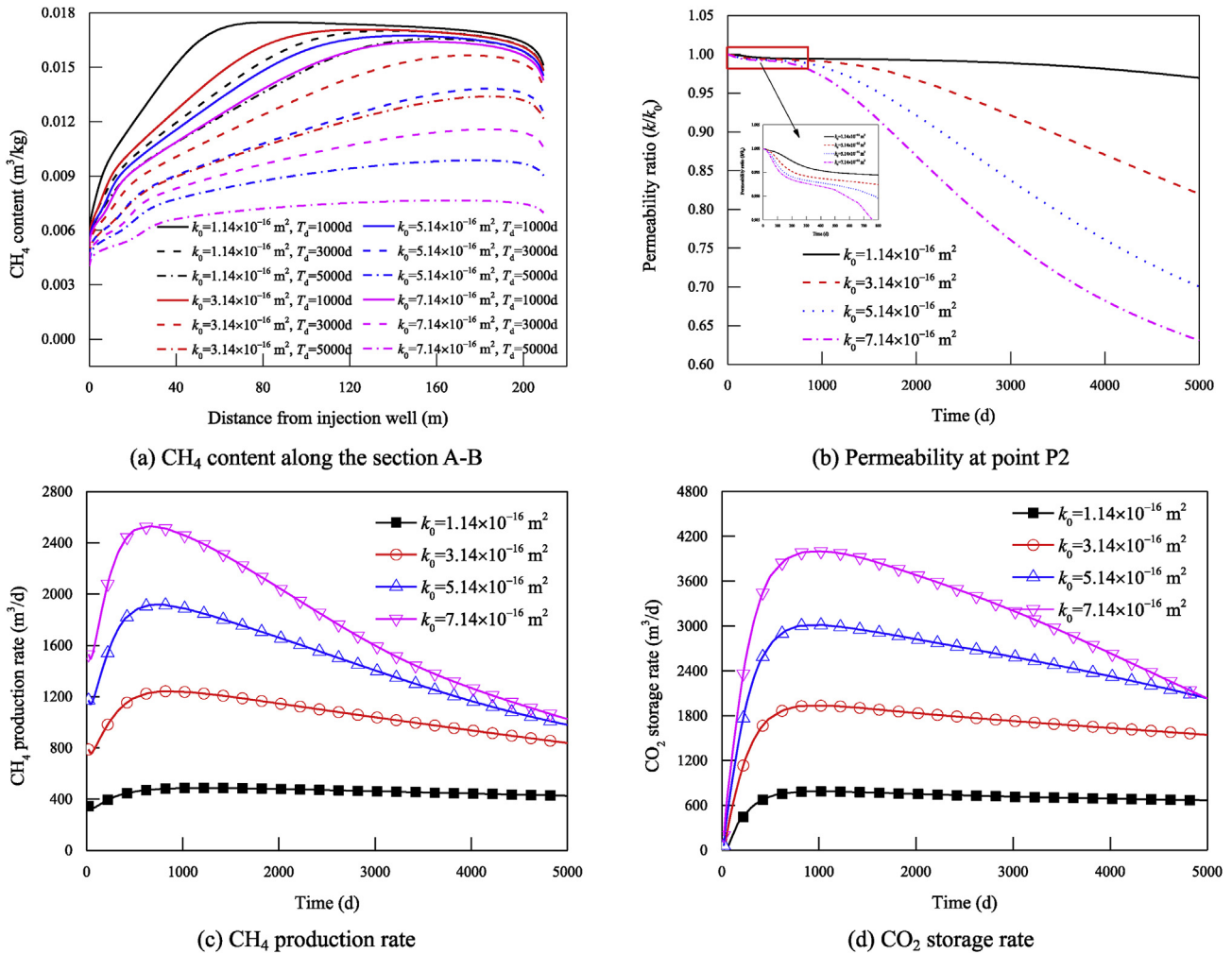

(c) CH₄ production rate

(d) CO₂ storage rate

Fig. 22. Variation of recovery, storage and permeability relative to different initial permeability.

permeability increases, leading to an increase in the resulting permeability. This increases the rate of transport of the fluid mixture, and thus gas production and storage rates, as shown in Fig. 22c and d. For initial permeabilities of 1.14, 3.14, 5.14, and $7.14 \times 10^{-16}\,\text{m}^2$, the peak production rates are 487, 1242, 1941 and 2530 m^3/d respectively, with corresponding peak storage rates of 787, 1933, 3011 and 3998 m^3/d.

6. Optimization of CO₂ injection start time

For CO_2-ECBM recovery may be optimized for the timing of the initial CO_2 injection. The timing of this injection may be immediately upon the initiation of production or it may be delayed. For the case of immediate initial injection, CO_2 is injected into the target coal seam as early as possible and will achieve maximum emission reduction. Associated challenges with this format are the risk of an early breakthrough of injected CO_2 in the production well, thereby decreasing the calorific value of produced gas and maybe necessitating cleaning, and the need for a high injection pressure to overcome water hindrance in the coal seam that is not yet dewatered [6]. Delayed injection of CO_2 can potentially resolve these issues, where the formation water is already depleted. Additionally, the possibility of CO_2 breakthrough is postponed until after the peak production rate when the majority of the high calorific CBM has already been recovered. Gas production will typically

ultimately cease because when an uneconomically high CO_2 concentration results at production. Similarly, CH₄ production can not be significantly improved when CO_2 injection is significantly delayed during primary recovery, where the reservoir pressure and average production rates have already been dramatically reduced. From this perspective, a rational timing of the initiation of injection should be defined.

Fig. 23 shows the simulated CH₄ production rates and CO_2 recycled rates for different injection start times. Compared to primary recovery alone, the CH₄ production rates for enhanced recovery are improved for all injection start times. For successively delayed injection, two peaks occur in the CH₄ production rates, with the first peak caused by primary recovery and the second peak resulting from CO_2 injection. When the injection start time is < 1000 days, the peak production rate due to enhanced recovery is larger than that due to primary recovery. Subsequent to this, the drop in the reservoir pressure gradient, decreases peak production rate over that of primary recovery. The production well should be shut down when the CO_2 concentration reaches a uneconomical magnitude. Here, we define this threshold as the ratio of CO_2 recovery rate to CH₄ production is 15%. Accordingly, for the studied case, the times to cease production for injection start times of 0 and 3000 days are 4320, and 7400 days respectively.

In Fig. 24, CH₄ cumulative productions progressively increase for the earlier application of CO_2 injection. When the production
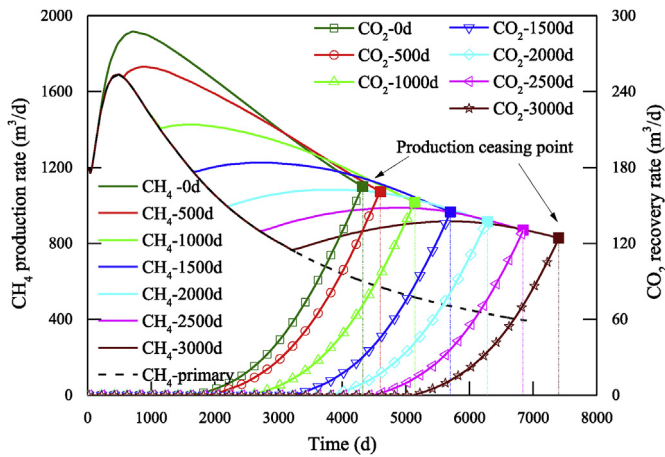
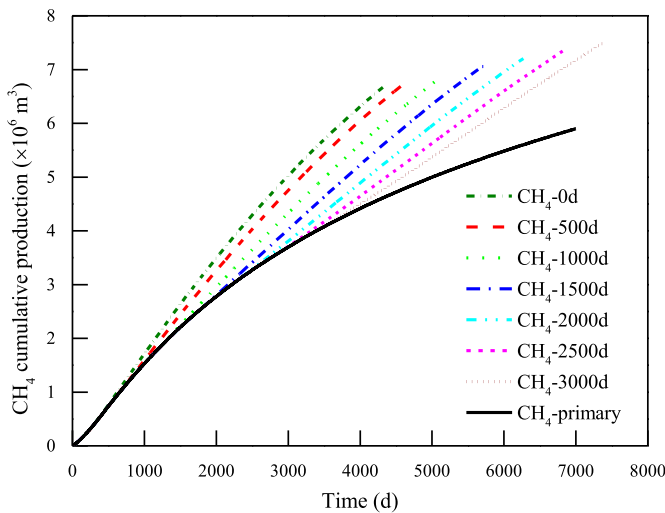Fig. 23. CH$_4$ production and CO$_2$ recovery rates for different injection start times.

Fig. 24. CH$_4$ cumulative production for different injection start times.
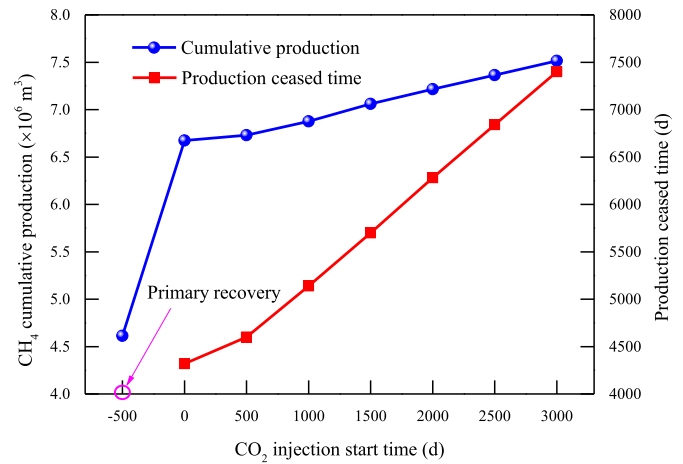

Fig. 25. Maximum cumulative production and ceasing times for different injection start times.
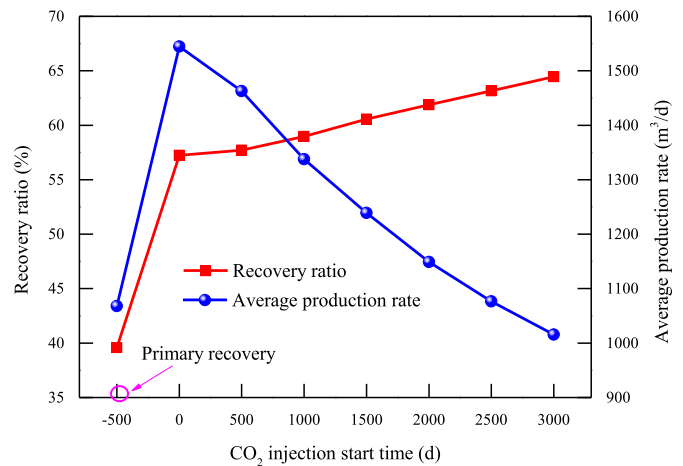
Fig. 26. Relationship between the recovery ratio, average production rate and injection start times.

reaches the time for cessation, the maximum cumulative production for injection start times of 0, 500, 1000, 1500, 2000, 2500, and 3000 days are 6.67, 6.73, 6.88, 7.06, 7.22, 7.36, and 7.51 million m^3 respectively. Taking the ceasing time of 4320 days as a reference, the corresponding cumulative production of primary recovery is 4.61 million m^3. Fig. 25 shows that cumulative production increases with an increasing delay in the injection start time − with a quasi-linear form.

The recovery ratio and average production rate are calculated and plotted in Fig. 26. This illustrates that the recovery ratio increases with an increased delay in the injection start time, but conversely decreases the average production rate. Postponing the initiation of injection returns a higher recovery ratio and also a lower average production rate. Considering the economic benefits, we define the optimum injection start time as the critical time when the average production rate is greater than that of primary recovery at the time of cessation. Here, the cessation time of the initial injection is 4320 days, and the corresponding recovery ratio and average production rate for primary recovery are 39.6% and 1068 m^3/d. The average production rate for injection start times of 2500 and 3000 days are 1077 and 1016 m^3/d, respectively. Therefore, the optimum injection start time is 2500 days for this particular demonstration project. The corresponding recovery ratio

is 63.2%, increased by 10.3% of initial injection.

Note that the optimum injection start time will vary for different sites and geological conditions, well spacing, CO$_2$ injection pressures and temperatures and other parameters, including the definition of economic conditions controlling the recovery. Regardless, an optimal start time for CO$_2$ injection may be both defined and determined, depending on the desired imposed constraints.

7. Conclusions

In this study, a thermo-hydro-mechanical-chemical model coupling the responses of non-isothermal competitive sorption of binary gas (CO$_2$, CH$_4$), two phase flow, thermal expansion and permeability evolution is developed. The model is first validated, then applied to analyze the coupling relations and key factors controlling CO$_2$-ECBM recovery. Finally, the model is used to optimize the injection start time that maximizes CH$_4$ recovery. The following conclusions are drawn:

(1) Injection of CO$_2$ is confirmed to have a net positive impact in promoting CBM recovery. The injected CO$_2$ indeed displaces CH$_4$ through competitive sorption and promotes CH$_4$ migration from the coal reservoir to the production well. The

peak production rate for enhanced recovery is both elevated and delayed compared with primary recovery, alone. For the modeled and extended case of this demonstration project, the recovery ratio (5000 d) for primary recovery is 43.8% of total inventory (GIP) relative to 63.3% for enhanced recovery - an enhancement of 1.45.

(2) Permeability evolution is shown to be the competitive result of matrix shrinkage/swelling induced by CH_4/CO_2 de/adsorption, expansion by temperature increase and compaction by the change in effective stress. During CO_2-ECBM recovery, the permeability first decreases due to the increase of effective stress (pressure depletion), rebounds through the initial value due to desorption of CH_4, before the arrival of CO_2 results in the continuous decrease to a very low magnitude.

(3) Four-way THMC couplings, either incorporating or absent heat transfer and/or two phase flow, are shown to significantly impact CO_2-ECBM recovery. The presence of formation water initially blocks CH_4 migration, leading to an increase in production rate at the reservoir is dewatered. The effect of warming by the high temperature of the injected CO_2 flux, together with the energy released by CO_2 adsorption, promotes CH_4 desorption, and conversely decelerates CO_2 adsorption. As a consequence, ignoring the impact of water migration (H) overestimates gas production, and ignoring the impact of heat transfer (T) underestimates gas production.

(4) The production behavior of CO_2-ECBM is largely controlled by several key factors. Higher injection pressure and/or initial permeability greatly promotes the transport of the fluid mixture, leading to an increase in CH_4 production and CO_2 sequestration. However, the warming effect reduces the adsorption capacity of CO_2, and coal seams with high water saturations take an extended period to dewater, and thus greater injection temperature and/or initial water saturation will result in a decrease in both CH_4 production and CO_2 sequestration.

(5) The selection of an optimal (delayed) start time for CO_2 injection can overcome the negative impacts of early breakthrough of CO_2, water hindrance and low average production of CH_4. For studied case, the optimum injection start time is 2500 days, with corresponding recovery ratio of 63.2%.

Notes

Acknowledgment

References

[1] Bertrand F, Cerfontaine B, Collin F. A fully coupled hydro-mechanical model for the modeling of coalbed methane recovery. J Nat Gas Sci Eng 2017;46: 307–25.

[2] Guan C, Liu S, Li C, Wang Y, Zhao Y. The temperature effect on the methane and CO2 adsorption capacities of Illinois coal. Fuel 2018;211:241–50.

[3] Li S, Fan C, Han J, Luo M, Yang Z, Bi H. A fully coupled thermal-hydraulic-mechanical model with two-phase flow for coalbed methane extraction. J Nat Gas Sci Eng 2016;33:324–36.

[4] Van Bergen F, Gale J, Damen KJ, Wildenborg AFB. Worldwide selection of early opportunities for CO2-enhanced oil recovery and CO2-enhanced coal bed methane production. At Energy 2004;29(9–10):1611–21.

[5] White CM, Smith DH, Jones KL, Goodman AL, Jikich SA, LaCount RB, Schroeder KT. Sequestration of carbon dioxide in coal with enhanced coalbed methane recovery a review. Energy Fuel 2005;19(3):659–724.

[6] Van Bergen F, Tambach T, Pagnier H. The role of CO2-enhanced coalbed methane production in the global CCS strategy. Energy Procedia 2011;4: 3112–6.

[7] Zhou F, Hou W, Allinson G, Wu J, Wang J, Cinar Y. A feasibility study of ECBM recovery and CO2 storage for a producing CBM field in Southeast Qinshui Basin, China. Int J Greenh Gas Contr 2013;19:26–40.

[8] Durucan S, Shi JQ. Improving the CO2 well injectivity and enhanced coalbed methane production performance in coal seams. Int J Coal Geol 2009;77: 214–21.

[9] Pan Z, Connell LD, Camilleri M. Laboratory characterisation of coal reservoir permeability for primary and enhanced coalbed methane recovery. Int J Coal Geol 2010;82(3–4):252–61.

[10] Wu Y, Liu J, Elsworth D, Chen Z, Connell L, Pan Z. Dual poroelastic response of a coal seam to CO2 injection. Int J Greenh Gas Contr 2010;4(4):668–78.

[11] Intergovernmental Panel on Climate Change (IPCC). The IPCC special report on carbon dioxide capture and storage. Cambridge: Cambridge University Press; 2005.

[12] Ross HE, Hagin P, Zoback MD. CO2 storage and enhanced coalbed methane recovery: reservoir characterization and fluid flow simulations of the BIG George coal, powder river basin, Wyoming, USA. Int J Greenh Gas Contr 2009;3(6):773–86.

[13] Wong S, Law D, Deng X, Robinson J, Kadatz B, Gunter WD, Zhiqiang F. Enhanced coalbed methane and CO2 storage in anthracitic coals—micro-pilot test at South Qinshui, Shanxi, China. Int J Greenh Gas Contr 2007;1(2): 215–22.

[14] Zarrouk SJ, Moore TA. Preliminary reservoir model of enhanced coalbed methane (ECBM) in a subbituminous coal seam, Huntly Coalfield, New Zealand. Int J Coal Geol 2009;77(1–2):153–61.

[15] Shi JQ, Durucan S, Fujioka M. A reservoir simulation study of CO2 injection and N2 flooding at the Ishikari coalfield CO2 storage pilot project, Japan. Int J Greenh Gas Contr 2008;2(1):47–57.

[16] Das S, Dutta P. Preliminary Understanding of CO2 sequestration and enhanced methane recovery in Raniganj coalfield of India by reservoir simulation. Energy Procedia 2017;114:4643–57.

[17] Vishal V, Singh TN, Ranjith PG. Influence of sorption time in CO2-ECBM process in Indian coals using coupled numerical simulation. Fuel 2015;139:51–8.

[18] Van Bergen F, Pagnier H, Krzystolik P. Field experiment of enhanced coalbed methane-CO2 in the upper Silesian basin of Poland. Environ Geosci 2006;13(3):201–24.

[19] Masoudian MS. Multiphysics of carbon dioxide sequestration in coalbeds: a review with a focus on geomechanical characteristics of coal. J Rock Mech Geotech Eng 2016;8(1):93–112.

[20] Liu Z, Cheng Y, Wang Y, Wang L, Li W. Experimental investigation of CO2 injection into coal seam reservoir at in-situ stress conditions for enhanced coalbed methane recovery. Fuel 2019;236:709–16.

[21] Wang L, Wang Z, Li K, Chen H. Comparison of enhanced coalbed methane recovery by pure N2 and CO2 injection: experimental observations and numerical simulation. J Nat Gas Sci Eng 2015;23:363–72.

[22] Yin G, Deng B, Li M, Zhang D, Wang W, Li W, Shang D. Impact of injection pressure on CO2−enhanced coalbed methane recovery considering mass transfer between coal fracture and matrix. Fuel 2017;196:288–97.

[23] Zhou F, Hussain F, Cinar Y. Injecting pure N2 and CO2 to coal for enhanced coalbed methane: experimental observations and numerical simulation. Int J Coal Geol 2013;116:53–62.

[24] Mazzotti M, Pini R, Storti G. Enhanced coalbed methane recovery. J Supercrit Fluids 2009;47(3):619–27.

[25] Jamshidi M, Jessen K. Water production in enhanced coalbed methane operations. J Petrol Sci Eng 2012;92:56–64.

[26] Pan Z, Ye J, Zhou F, Tan Y, Connell LD, Fan J. CO2 storage in coal to enhance coalbed methane recovery: a review of field experiments in China. Int Geol Rev 2018;60(5–6):754–76.

[27] Pan Z, Connell LD. Modelling permeability for coal reservoirs: a review of analytical models and testing data. Int J Coal Geol 2012;92:1–44.

[28] Masoudian MS, Airey DW, El-Zein A. The role of coal seam properties on coupled processes during CO2 sequestration: a parametric study. Greenh Gas Sci Tech 2016;6(4):492–518.

[29] Masoudian MS, Airey DW, El-Zein A. Experimental investigations on the effect of CO2 on mechanics of coal. Int J Coal Geol 2014;128:12–23.

[30] Masoudian MS. Chemo-hydro-mechanical aspects of CO2 sequestration in deep coal seams. Sydney, Australia: University of Sydney; 2013.

[31] Gong B, Zhang Y, Fan Y, Qin G. A novel approach to model enhanced coal bed methane recovery with discrete fracture characterizations in a geochemical simulator. J Petrol Sci Eng 2014;124:198—208.

[32] Liu T, Lin B, Yang W, Zhai C, Liu T. Coal permeability evolution and gas migration under non-equilibrium state. Transport Porous Media 2017;118(3): 393—416.

[33] Xia T, Zhou F, Liu J, Hu S, Liu Y. A fully coupled coal deformation and compositional flow model for the control of the pre-mining coal seam gas extraction. Int J Rock Mech Min Sci 2014;72:138—48.

[34] Zhou L, Feng Q, Chen Z, Liu J. Modeling and upscaling of binary gas coal interactions in CO2 enhanced coalbed methane recovery. Procedia Environ Sci 2012;12:926—39.

[35] Wang G, Li W, Wang P, Yang X, Zhang S. Deformation and gas flow characteristics of coal-like materials under triaxial stress conditions. Int J Rock Mech Min Sci 2017;91:72—80.

[36] Liu T, Lin B, Yang W, Liu T, Kong J, Huang Z, Zhao Y. Dynamic diffusion-based multifield coupling model for gas drainage. J Nat Gas Sci Eng 2017;44:233—49.

[37] Sun X, Zhang Y, Li K, Gai Z. A new mathematical simulation model for gas injection enhanced coalbed methane recovery. Fuel 2016;183:478—88.

[38] Liu T, Lin B, Yang W. Impact of matrix—fracture interactions on coal permeability: model development and analysis. Fuel 2017;207:522—32.

[39] Zhao Y, Hu Y, Zhao B, Yang D. Nonlinear coupled mathematical model for solid deformation and gas seepage in fractured media. Transport Porous Media 2004;55(2):119—36.

[40] Wang G, Chu X, Yang X. Numerical simulation of gas flow in artificial fracture coal by three-dimensional reconstruction based on computed tomography. J Nat Gas Sci Eng 2016;34:823—31.

[41] Connell LD, Detournay C. Coupled flow and geomechanical processes during enhanced coal seam methane recovery through CO2 sequestration. Int J Coal Geol 2009;77(1—2):222—33.

[42] Wei Z, Zhang D. Coupled fluid-flow and geomechanics for triple-porosity/dualpermeability modeling of coalbed methane recovery. Int J Rock Mech Min Sci 2010;47(8):1242—53.

[43] Yao S, Pini R, Wang X, Zeng F, Ju N. Computational fluid dynamics modeling of slip flow coupled with gas adsorption/desorption kinetics in complex pore space. In: SPE annual technical conference and exhibition. Society of Petroleum Engineers; 2018.

[44] Clarkson CR, Qanbari F. Transient flow analysis and partial water relative permeability curve derivation for low permeability undersaturated coalbed methane wells. Int J Coal Geol 2015;152:110—24.

[45] Ma T, Rutqvist J, Oldenburg CM, Liu W, Chen J. Fully coupled two-phase flow and poromechanics modeling of coalbed methane recovery: impact of geomechanics on production rate. J Nat Gas Sci Eng 2017;45:474—86.

[46] Kumar H, Elsworth D, Mathews JP, Liu J, Pone D. Effect of CO2 injection on heterogeneously permeable coalbed reservoirs. Fuel 2014;135:509—21.

[47] Zhu WC, Wei CH, Liu J, Qu HY, Elsworth D. A model of coal—gas interaction under variable temperatures. Int J Coal Geol 2011;86(2):213—21.

[48] Ren T, Wang G, Cheng Y, Qi Q. Model development and simulation study of the feasibility of enhancing gas drainage efficiency through nitrogen injection. Fuel 2017;194:406—22.

[49] Liu J, Li G, Zhang Y. Numerical simulation of CO2 flooding of coalbed methane considering the fluid-solid coupling effect. PLoS One 2016;11(3):e0152066.

[50] Rutqvist J, Wu YS, Tsang CF, Bodvarsson G. A modeling approach for analysis of coupled multiphase fluid flow, heat transfer, and deformation in fractured porous rock. Int J Rock Mech Min Sci 2002;39(4):429—42.

[51] Wu Y, Liu J, Chen Z, Elsworth D, Pone D. A dual poroelastic model for CO2-enhanced coalbed methane recovery. Int J Coal Geol 2011;86(2):177—89.

[52] Fan Y, Deng C, Zhang X, Li F, Wang X, Qiao L. Numerical study of CO2-enhanced coalbed methane recovery. Int J Greenh Gas Contr 2018;76:12—23.

[53] Teng T, Zhao Y, Gao F, Wang JG, Wang W. A fully coupled thermo-hydro-mechanical model for heat and gas transfer in thermal stimulation enhanced coal seam gas recovery. Int J Heat Mass Transf 2018;125:866—75.

[54] Masoudian MS, Airey DW, El-Zein A. A chemo-poro-mechanical model for sequestration of carbon dioxide in coalbeds. Geotechnique 2013;63(3): 235—43.

[55] Zhang XG, Ranjith PG, Perera MSA, Ranathunga AS, Haque A. Gas transportation and enhanced coalbed methane recovery processes in deep coal seams: a review. Energy Fuel 2016;30(11):8832—49.

[56] Lin J, Ren T, Wang G, Nemcik J. Simulation investigation of N2-injection enhanced gas drainage: model development and identification of critical parameters. J Nat Gas Sci Eng 2018;55:30—41.

[57] Collin F, Li XL, Radu JP, Charlier R. Thermo-hydro-mechanical coupling in clay barriers. Eng Geol 2002;64(2—3):179—93.

[58] Fan CJ, Li S, Luo MK, Yang ZH, Lan TW. Numerical simulation of hydraulic fracturing in coal seam for enhancing underground gas drainage. Energy Explor Exploit 2019;37(1):166—93.

[59] Corey AT. The interrelation between gas and oil relative permeability. Prod Mon 1954;31:533—46.

[60] Clarkson CR, Rahmanian M, Kantzas A, Morad K. Relative permeability of CBM reservoirs: controls on curve shape. Int J Coal Geol 2011;88(4):204—17.

[61] Xu H, Tang DZ, Tang SH, Zhao JL, Meng YJ, Tao S. A dynamic prediction model for gas—water effective permeability based on coalbed methane production data. Int J Coal Geol 2014;121:44—52.

[62] Xia T, Zhou F, Gao F, Kang J, Liu J, Wang J. Simulation of coal self-heating processes in underground methane-rich coal seams. Int J Coal Geol 2015;141:1—12.

[63] Biot MA. General theory of three-dimensional consolidation. J Appl Phys 1941;12(2):155—64.

[64] Durucan S, Ahsanb M, Shia JQ. Matrix shrinkage and swelling characteristics of European coals. Energy Procedia 2009;1(1):3055—62.

[65] Cui X, Bustin RM. Volumetric strain associated with methane desorption and its impact on coalbed gas production from deep coal seams. AAPG Bull 2005;89(9):1181—202.

[66] Hol S, Gensterblum Y, Massarotto P. Sorption and changes in bulk modulus of coal—experimental evidence and governing mechanisms for CBM and ECBM applications. Int J Coal Geol 2014;128:119—33.

[67] Chen M, Chen Z. Effective stress laws for multi-porosity media. Appl Math Mech Engl. 1999;20:1207—13.

[68] Wang G, Wang K, Wang S, Elsworth D, Jiang Y. An improved permeability evolution model and its application in fractured sorbing media. J Nat Gas Sci Eng 2018;56:222—32.

[69] Wu Y, Pan Z, Zhang D, Lu Z, Connell LD. Evaluation of gas production from multiple coal seams: a simulation study and economics. Int J Min Sci Technol 2018;28:359—71.

[70] Zheng C, Lin B, Kizil MS, Aminossadati SM, Li H, Chen Z. Analysis on the multiphase flow characterization in cross-measure borehole during coal hydraulic slotting. Int J Min Sci Technol 2018;28:701—5.

[71] Song Y, Jiang B, Lan FJ. Competitive adsorption of CO2/N2/CH4 onto coal vitrinite macromolecular: effects of electrostatic interactions and oxygen functionalities. Fuel 2019;235:23—38.

[72] Song Y, Jiang B, Qu MJ. Molecular dynamic simulation of self-and transport diffusion for CO2/CH4/N2 in low-rank coal vitrinite. Energy Fuel 2018;32(3): 3085—96.

Nomenclature

a: width of coal matrix
b: facture aperture
b_k: Klinkenberg factor
c_1: thermal coefficient of gas sorption
c_2: thermal coefficient of gas sorption
C_{g1}: specific heat capacity of CH_4
C_{g2}: specific heat capacity of CO_2
C_s: specific heat capacity of coal skeleton
C_v: specific heat capacity of vapor
C_w: specific heat capacity of water
D: effective elastic modulus
D_i: diffusion coefficient of gas component i
E: elastic modulus
E_s: skeleton elastic modulus
F_k: body force in the k direction
G: shear modulus
h: relative humidity
H_{gi}: Henry's coefficient of gas component i
k: absolute permeability of coal seam
K: bulk modulus
k_0: initial fracture permeability
K_n: normal stiffness of fracture
k_{rg}: gas relative permeability
k_{rg0}: endpoint relative permeability of gas
k_{rw}: water relative permeability
k_{rw0}: endpoint relative permeability of water
K_s: skeleton bulk modulus
L: cleat spacing
M_{gi}: molar mass of gas component i
m_{mgi}: gas mass in one volume of coal matrix
N: number of gas components in mixture
p_{cgw}: capillary pressure
p_f: water-gas mixture pressure in fracture
p_{fgi}: gas pressure of component i in fracture
p_{fw}: water pressure in fractures
p_{gi}: gas pressure of component i
p_{Li}: Langmuir pressure constant of gas component i
p_m: gas mixture pressure in matrix
p_{mgi}: gas pressure of component i in matrix
p_s: atmospheric pressure
q_{gi}: velocity of gas component i
q_{sti}: isosteric heat of gas adsorption of component i
q_w: velocity of water
R: gas molar constant
r_a: ratio of matrix width to the REV length
R_v: constant of vapour
s: length of the REV
s_g: gas saturation
s_{gr}: residual gas saturation
s_w: water saturation

s_{wr}: irreducible water saturation
T: temperature of coal seam
t: time
T_0: initial temperature in coal seam
T_{ref}: reference temperature for adsorption test
T_s: temperature under standard condition
u_k: deformation in the k direction
V_{Li}: Langmuir volume constant of gas component i
V_{sgi}: absorbed gas content
x_i: molar fraction of gas component i
α_f: Biot effective stress coefficient for fractures
α_m: Biot effective stress coefficient for pressure in coal matrix
α_T: thermal expansion coefficient
δ_{ij}: Kronecker delta with 1 for $i=j$ and 0 for $i\neq j$
ε_{Li}: Langmuir-type strain coefficient
ε_s: volumetric strain induced by gas sorption
ε_v: volume strain of coal
$(\rho C_p)_{eff}$: effective specific heat capacity of coal mass
η_{eff}: effective heat convection coefficient of mixture fluid
λ_{eff}: effective thermal conductivity of coal mass
λ_{fgm}: thermal conduction coefficients for gas mixture in fracture
λ_{fwm}: thermal conduction coefficients for liquid mixture in fracture
λ_i: thermal conduction coefficient of gas component i

λ_{mgm}: thermal conduction coefficients for gas mixture in matrix
λ_s: thermal conduction coefficients for coal skeleton
μ_{gi}: dynamic viscosity of gas component i
μ_w: dynamic viscosity of water
ν: Poisson's ratio
ρ_{fv0}: density of saturated vapour
ρ_{gi}: density of gas component i
ρ_{gsi}: density of gas component i at standard condition
ρ_s: density of coal skeleton
ρ_w: water density
τ_i: desorption time of gas component i
φ_f: porosity of fracture
φ_{f0}: initial fracture porosity
φ_m: porosity in coal matrix

Subscript

0: initial value of the variable
m: matrix
f: fracture
i: gas component, $i=1$ for CH_4, $i=2$ for CO_2